

# **First Principle Study of Sn doped V<sub>2</sub>O<sub>5</sub> with Oxygen Vacancy as Cathode Material for Magnesium Batteries**

A Thesis

submitted towards the partial fulfilment for the award of the degree of

**INTEGRATED MASTER OF SCIENCE IN PHYSICS**

Submitted by

**AASIF MAJEED**

(Reg. No: I160201)

Under the guidance of

**Dr.P.RAVINDRAN**

**Professor**

**Department of Physics, CUTN**



**DEPARTMENT OF PHYSICS**

**SCHOOL OF BASIC AND APPLIED SCIENCES**

**CENTRAL UNIVERSITY OF TAMIL NADU**

**THIRUVARUR**

**MAY-2021**

## **DECLARATION**

This is to certify that this project thesis, entitled "***First Principle Study of Sn doped V<sub>2</sub>O<sub>5</sub> with Oxygen Vacancy as Cathode Material for Magnesium Batteries***" which is submitted by me towards the partial fulfilment of the requirements for the award of the degree of *Integrated Master of Science(Physics)* to the Central University of Tamil Nadu, comprises only my original work and due acknowledgement has been made in the text to all other materials used.

**Date:** \_\_\_\_\_ **Signature of the Candidate**

**Place:** Thiruvarur



தமில்நாடு கேந்திய விஶ்வவி஦்யாலய  
(संसद द्वारा पारित अधिनियम 2009 के अंतर्गत स्थापित)  
CENTRAL UNIVERSITY OF TAMIL NADU  
(Established by an Act of Parliament, 2009)



## Certificate

This is to certify that this project entitled "***First Principle Study of Sn doped V<sub>2</sub>O<sub>5</sub> with Oxygen Vacancy as Cathode Material for Magnesium Batteries***" submitted in partial fulfilment of the degree of INTEGRATED MASTERS IN SCIENCE (Physics) to the Central University of Tamil Nadu, done by **Aasif Majeed, Register No.: I160201**, is an authentic work carried out by him at Department of Physics, Central University of Tamil Nadu under my guidance. The matter embodied in this project work has not been submitted earlier for award of any degree or diploma to the best of my knowledge and belief.

Date:

Project supervisor

place: Thiruvarur

Prof.P.Ravindran

Head of the department

Project coordinator

Dr.L.Kavitha

Dr.R.Arun

## Acknowledgment

I would like to express my deepest gratitude to my advisor, **Prof. P. Ravindran**, Professor, School of Basics and Applied Sciences, Central University of Tamil Nadu, for his excellent guidance, patience, and providing me with an excellent atmosphere for doing research.

I convey my gratitude to **Prof. L. Kavitha**, Head of the Department, Department of Physics, Central University of Tamil Nadu, for giving me such a constructive opportunity to do this thesis work in department of Physics.

I also thank **Mr. Vishnu Sudharshanam** for guiding me and clearing my doubts constantly. I would like to express my thanks to the other research scholars in my laboratory **Mr. Mukesh Kumar**, **Miss S Kiruthika**, **Miss Anu Maria Augustine**, **Mr. Suresh R Lawrence**, and **Kruthika** for their valuable support and encouragement. I would like to give special thanks to **Mr. Irfan Ahmad Lone**, **Mr. Amal raj V**, **Mr. Ravi Kaushik**, **Mr. Hakim Jahan**, **Miss Ramyaa RR** and **Miss Kavya H** for their constant support, in all my struggles. I would like to thank all my dear friends, in Department of physics, Central University of Tamil Nadu, for their good support. Also I thank my family, for always being there for me.

## Abstract

Due to the demand for renewable energy resources energy storage has gained more importance in today's life. For efficient utilization of Renewable energies, batteries are playing main role in energy storages. By considering the limitations of Lithium ion batteries new battery chemistries based on the multivalent working ions have been proposed. Among them Magnesium batteries have gained huge attention as a promising green alternative for practical applications. However the search for cathode materials with high energy density and good rate capability is still in demand for these batteries.  $V_2O_5$  is one of the few cathode materials in which magnesium reversibility is possible. The sluggish kinetics of  $Mg^{2+}$  ions in this material hinder its performance in practical applications. Here in this work we used the first principle calculations to study the impact of Sn doping in this material. Density functional theory (DFT+U) calculations in combination with VdW-DF was carried out to study the lattice structure and electronic structure of pristine and Sn doped  $V_2O_5$  system. VdW-DF method was found to be more accurate for predicting the interlayer spacing and bandgaps. It is found that the electrical conductivity of pristine  $V_2O_5$  is enhanced by Sn doping along with an oxygen vacancy. Also, NEB calculations are done to study the role of Sn doping on the diffusivity of  $Mg^{2+}$  ions. It is found that the diffusion barrier is higher in the disordered layer where as it is reduced in the upper layer. Thus, dopants with oxygen vacancy can be utilized for opening formerly closed diffusion channels in  $V_2O_5$  and this may be improved further by more in-depth studies.

# Contents

|   |           |
|---|-----------|
| <i>Acknowledgments</i> . . . . .  | 4         |
| <b>Abstract</b> . . . . .   | 5         |
| <b>1 Introduction</b>   | <b>11</b> |
| 1.1 Battery systems . . . . .   | 12        |
| 1.1.1 How Battery works? . . . . .                                      | 12        |
| 1.1.2 Battery Anodes . . . . .  | 13        |
| 1.1.3 Battery Cathodes . . . . .  | 13        |
| 1.2 Lithium-ion Battery . . . . .                                       | 15        |
| 1.3 Advantages and limitations of using lithium ion batteries . . . . . | 17        |
| 1.4 Beyond lithium ion Batteries . . . . .                              | 17        |
| 1.4.1 Alloying compounds: Li-Si and Li-S . . . . .                      | 18        |
| 1.4.2 Na-ion . . . . .  | 18        |
| 1.4.3 Multivalent working ions . . . . .                                | 19        |
| <b>2 Rechargeable Magnesium Battery</b>                                 | <b>21</b> |
| 2.1 Recent advances in Electrolytes and Anodes . . . . .                | 22        |
| 2.2 Cathodes . . . . .  | 23        |
| 2.2.1 Molybdenum sulfide . . . . .                                      | 23        |
| 2.2.2 Layered Structure Cathode Materials . . . . .                     | 25        |
| 2.2.3 Spinel Structure Cathode Materials . . . . .                      | 27        |
| 2.2.4 Polyanionic Compounds . . . . .                                   | 27        |
| <b>3 Theoretical Background</b>   | <b>29</b> |
| 3.1 Introduction to density functional theory . . . . .                 | 29        |
| 3.1.1 Electronic Structure Problem . . . . .                            | 30        |
| 3.1.2 Born-Oppenheimer Approximation . . . . .                          | 31        |
| 3.1.3 Wave Function Based Methods . . . . .                             | 32        |

|          |   |           |
|----------|---|-----------|
| 3.1.4    | Density-Functional Theory . . . . .   | 34        |
| 3.2      | Transition State Search Methods . . . . .   | 41        |
| 3.2.1    | Nudged Elastic Band Method . . . . .  | 41        |
| 3.2.2    | The Dimer Method . . . . .  | 44        |
| 3.3      | First Principle Calculations of Battery Properties . . . . .  | 45        |
| 3.3.1    | Intercalation/Deintercalation Voltage . . . . .   | 45        |
| 3.3.2    | Ionic Diffusivity . . . . .   | 46        |
| <b>4</b> | <b>Computational Details</b>  | <b>48</b> |
| 4.1      | Introduction to VASP . . . . .  | 48        |
| 4.2      | Methodology . . . . .   | 50        |
| <b>5</b> | <b>First Principle Study of Sn doped V<sub>2</sub>O<sub>5</sub> with Oxygen Vacancy as Cathode Material for Magnesium Batteries</b> | <b>51</b> |
| 5.1      | Literature review . . . . .   | 51        |
| 5.1.1    | Introduction . . . . .  | 51        |
| 5.1.2    | Polymorphs of V <sub>2</sub> O <sub>5</sub> . . . . .   | 52        |
| 5.1.3    | Effect of Sn-doping in V <sub>2</sub> O <sub>5</sub> Cathode Materials . . . . .  | 53        |
| 5.2      | Results and Discussions . . . . .   | 54        |
| 5.2.1    | Structural Details . . . . .  | 54        |
| 5.2.2    | Electronic Structure . . . . .  | 55        |
| 5.3      | Activation Barrier for Mg Diffusion and Effect of Sn doping . . . . .   | 57        |
| 5.4      | Mg-ion Diffusivity . . . . .  | 60        |
| <b>6</b> | <b>Conclusions and Future Outlook</b>   | <b>61</b> |
|          | References . . . . .  | 70        |

# List of Figures

|  |    |
|--|----|
| 1.1.1 a) The theoretical capacity of graphite and various metal anodes. b) Reduction potential of various metal anodes. c) The elemental abundance in the crust. . . . .   | 14 |
| 1.1.2 an overview of the average discharge potentials and specific capacities for all types of electrodes. . . . .   | 14 |
| 1.2.1 Rhombohedral structure of LiCoO <sub>2</sub> . Co octahedra shown in blue, Li octahedra in green and the oxygen stacking is indicated by A, B and C. . . . .   | 16 |
| 1.2.2 List of representative electrode materials and electrolyte types investigated for rechargeable non-aqueous Li-ion batteries . . . . .  | 16 |
| 1.4.1 Number of publications from 1985 until 2015 featuring multivalent electrochemistry. The pie chart corresponds to the distribution of this research for different chemistries (Mg, Zn, Ca, etc.) . . . . .  | 20 |
| 2.0.1 The number of published papers related to magnesium batteries . . . . .  | 21 |
| 2.0.2 (a)Schematic diagram of typical electrochemical reaction process of MIBs with (Mg as anode, V <sub>2</sub> O <sub>5</sub> as cathode, PhMgCl–AlCl <sub>3</sub> /THF solution as electrolytes) (b)Theoretical capacity comparison between Li, graphite and Mg . . . . . | 22 |
| 2.2.1 Chevrel Phase Mo <sub>6</sub> S <sub>8</sub> crystallographic structure . . . . .  | 24 |
| 2.2.2 a)Inner-ring and outer-ring hopping between partially occupied outer and inner sites b)Charge/discharge curves and cycle performance of Mo <sub>6</sub> S <sub>8</sub> cathode containing different materials . . . . .  | 24 |
| 2.2.3 a)Crystallographic structure of crystallineVO <sub>5</sub> where Red pyramids indicate VO <sub>5</sub> polydera and the yellow atoms are intercalants b)Different polymorphs of V <sub>2</sub> O <sub>5</sub> . materials . . . . .                                    | 26 |
| 2.2.4 The crystal structures of Mn <sub>3</sub> . . . . .  | 27 |
| 3.2.1 A schematic representation of diffusion in between a stable site A and a stable site B. E <sub>A</sub> and E <sub>B</sub> are the activation barriers from site A and B respectively. . . . .  | 42 |

|   |    |
|---|----|
| 3.2.2 A schematic representation of the NEB method. The linear intepolation as the initial pathway, two simulation steps and the final optimized pathway are shown <sup>1</sup> . . . . .   | 43 |
| 3.2.3 Comparison of the result obtained by regular NEB and CI-NEB method for CH <sub>4</sub> dissociation on Ir(111) surface <sup>2</sup> . . . . .   | 44 |
| 5.1.1 Crystal structure of V <sub>2</sub> O <sub>5</sub> . Vanadium atoms are in brown color, while oxygen atoms are in red color <sup>3</sup> . . . . .  | 52 |
| 5.1.2 (a) $\alpha$ and (b) $\delta$ polymorphs of orthorhombic V <sub>2</sub> O <sub>5</sub> are shown along the c-axis.(c) along the a-axis which is compared to the (d) $\gamma$ polymorph, has a different orientation of VO <sub>5</sub> pyramids and the dashed blue rectangle in panel (c) indicates a distance of c/2 Panel (e) illustrates the $\epsilon$ phase. <sup>4</sup> . . . . . | 53 |
| 5.2.1 The total Energy vs Volume curve for (a) V <sub>2</sub> O <sub>5</sub> (b) $\alpha$ -MgV <sub>2</sub> O <sub>5</sub> . . . . .  | 54 |
| 5.2.2 Projected density of states (PDOS) of (a) $\alpha$ -V <sub>2</sub> O <sub>5</sub> where blue and red lines illustrate states contributed by O 2p and V 3d, respectively (b) $\alpha$ -MgV <sub>2</sub> O <sub>5</sub> . . . . .   | 56 |
| 5.2.3 PDOS of Sn doped V <sub>2</sub> O <sub>5</sub> supercell where red, black, and green lines represent states contributed by V, O , and Sn respectively (a) oxygen vacancy at O(1) site with one V atoms replaced (b) oxygen vacancy at O(2) site with two adjacent V atoms replaced  | 56 |
| 5.3.1 Three potential paths for Mg-ion hpopping in $\alpha$ -V <sub>2</sub> O <sub>5</sub> . . . . .  | 57 |
| 5.3.2 Migration Barriers for $\alpha$ -V <sub>2</sub> O <sub>5</sub> Path on the disordered layer (P <sub>1</sub> ) . . . . .   | 58 |
| 5.3.3 Migration Barriers for $\alpha$ -V <sub>2</sub> O <sub>5</sub> Path above the disordered layer(P <sub>2</sub> ) . . . . .   | 59 |

# List of Tables

|   |    |
|---|----|
| 1.4.1 Comparison of univalent and multivalent standard electrode potentials and theoretical<br>anode capacities . . . . .   | 19 |
| 5.2.1 Comparison of orthorhombic lattice constants a, b, c of bulk V <sub>2</sub> O <sub>5</sub> obtained from<br>experimental measurement versus those from the current calculations. The percentage<br>values give the relative deviation from the experimental value. All values are given in Å.                 | 55 |
| 5.2.2 Comparison of orthorhombic lattice constants a, b, c of bulk α-MgV <sub>2</sub> O <sub>5</sub> obtained<br>from experimental measurement versus those from the current calculations. The<br>percentage values give the relative deviation from the experimental value. All values<br>are given in Å . . . . . | 55 |
| 5.4.1 Calculated diffusivity of Mg <sup>2+</sup> . . . . .  | 60 |

# Chapter 1

## Introduction

Energy, being an important basis for social and economic development, is the most critical problem faced by current human society. With the rapid development of modern society, energy is playing an important role in human life. Meanwhile, protection of environment is also gaining a huge attention.<sup>5</sup> The limitations of traditional energy sources in terms of reserves, environmental pollution, energy efficiency, and cost have become increasingly prominent. Research of new alternatives of energy sources have been a common trend around the world, Renewable energy is regarded as an effective solution to these environmental problems, especially in reducing carbon emissions, which may be the best solution for coming human energy demand.<sup>6</sup>

The most commonly used renewable energy sources, such as wind, solar, hydroelectric and geothermal energies distribute unevenly in time and space, which give rise to the demands for energy storage devices.<sup>7</sup> For efficient utilization of renewable energies, batteries of various performance profiles are playing a vital role in storing and releasing the generated electrical energy.<sup>8</sup> Battery energy storage is the key to the large-scale development of renewable energy in recent years with the widespread application.<sup>6</sup>

The rechargeable lithium ion batteries (LIBs), lead acid batteries (LAB), and Supercapacitors are widely used as energy storage devices in various portable devices.<sup>9</sup> Among them Rechargeable (secondary) lithium battery is one of the most successful technologies that can reversely transform electric energy.<sup>10</sup> LIBs have dominated the current chemical energy storage market and have been increasingly employed in various devices due to their high energy density and portability.<sup>5</sup>

However, LIBs suffer from many disadvantages which includes its high cost and poor safety performance. Several nations have limited lithium deposits, necessitates research into energy storage technologies of abundant minerals.<sup>11</sup> So the limited distribution of lithium resources in the earth's

crust therefore, make it is crucial to develop new battery systems.<sup>12</sup>

In the following section we will be discussing the properties of different battery systems.

## 1.1. Battery systems

### 1.1.1. How Battery works?

A battery is device that is capable of converting its chemical energy contained in its material to electrical energy through redox reaction. The word “battery” was coined by Benjamin Franklin. While as Alessandro Volta, became the first person for inventing the first voltaic (or Battery).<sup>13</sup>

Batteries are made up of two electrodes, anode and cathode interconnected by an electrolyte, which is an ironically conductive substance. The electrode which gets oxidized during discharge is called the anode and the one which gets reduced during discharge is called the cathode. Electrolytes simply act as a bridge for ion transport by preserving charge balance. The chemical potentials of the two electrodes vary due to the chemistry that occurs at each end. The amount of electrical energy a battery can produce per mass or volume is a function of the cell’s voltage and capacity, which are determined by the chemistry of the system.<sup>14</sup>

The energy density (Whkg<sup>-1</sup>), specific energy(WhL<sup>-1</sup>), specific power (Wkg<sup>-1</sup>), cycle life, performance, and cost of a battery are the specific factors to consider.

The difference in chemical potentials between the two electrodes determines the open circuit voltage of the cell,  $V_{oc}$

$$V_{oc} = \frac{(\mu_a - \mu_c)}{e} \quad (1.1.1)$$

where  $\mu_a$  and  $\mu_c$  is the chemical potential of the anode and cathode respectively, and  $e$  is the charge of electron.

The theoretical capacity,  $Q$  of a cell is the amount of charge per unit mass (specific) or volume (volumetric) that can be transferred across the cell. For a given electrode the theoretical specific capacity can be calculated by

$$Q = \frac{\Delta x \times F \times 1000}{M_w \times 3600} \quad (1.1.2)$$

Where  $\Delta x$  is the number electrons transferred,  $F$  is the Faraday constant and  $M_w$  the molecular weight. The constant **1000** and **3600** give the capacity in units of mAh g<sup>-1</sup> (as the Faraday constant has units of sAmol<sup>-1</sup>).<sup>15 ,13</sup>

Power or the rate at which energy can be extracted from a cell, is another important property of

modern cells. This is the sum of the discharge voltage and the current drawn from the battery, and it is calculated in watts. The chemistry of the active material determines the power of a cell, which is a function of both cell design and an intrinsic property of the electrode material.<sup>14</sup>

Equation 1.1.3 is used to calculate the current required,  $I$ , to fully charge a mass of active material,  $m$  with capacity  $C$  in a given time,  $t$

$$I = \frac{Q \times m}{t} \quad (1.1.3)$$

### 1.1.2. Battery Anodes

Carbon materials have been used as electrodes in a variety of battery technologies for a long time. Sony Corporation developed the first prototype of LIBs in 1991, using graphite for Li<sup>+</sup> intercalation. Alkali elements like Li, Na, K contains loosely bounded outermost electron that makes them attractive as intercalants by forming an ionic bond.<sup>16</sup>

While lithium metal on the anode (negative electrodes) may provide high energy densities, its cycling can cause unwanted dendrites on the anode, which can penetrate the separator and cause an electrical short circuit. In comparison to every other intercalation-type anode materials, carbon has a promising combination of low cost, abundance, moderate energy density, power density, and cycle life.<sup>17</sup> This is further improved by the use of a metallic anode of the corresponding metals, as these metals do not form dendrites as in the case of Li metal. The energy densities and the reductive potentials of various metallic anodes are shown in Fig.1.1.1<sup>6</sup>

### 1.1.3. Battery Cathodes

Cathode materials, play a critical role in cell voltage and capacity, also account upto 40% to 50% of the battery cost. Furthermore many other factors, such as cycle life, rate capability, protection, cost and environmental friendliness are all influenced by cathode performance.<sup>18</sup>

In terms of their storage mechanism, cathode materials are divided into intercalation type cathodes and conversion type cathodes.

(A) INTERCALATION TYPE CATHODES : In Intercalation materials a guest moves between sites within a host network and the guest ions can be removed while maintaining the host structure. These intercalation compounds can further classified into several crystal structures, such as layered, spinel, olivine and favorite. Layered structure is the earliest form of cathode material used in lithium ion batteries.<sup>17</sup> we will further discuss these structure in different battery systems.

(B) CONVERSION TYPE CATHODES : During charging and discharging these materials use large amount of capacity released from chemical bond rupture and structural transformation.These phase

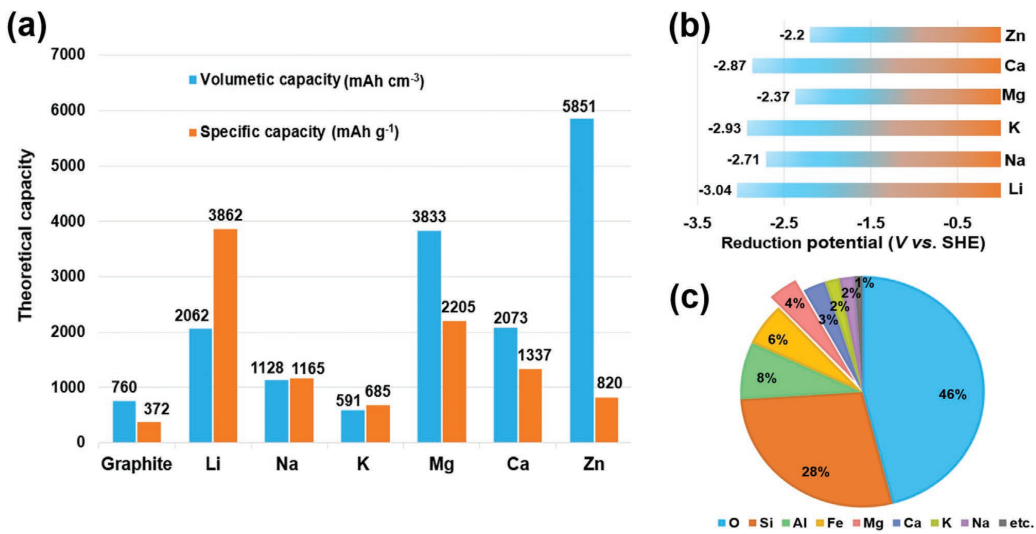
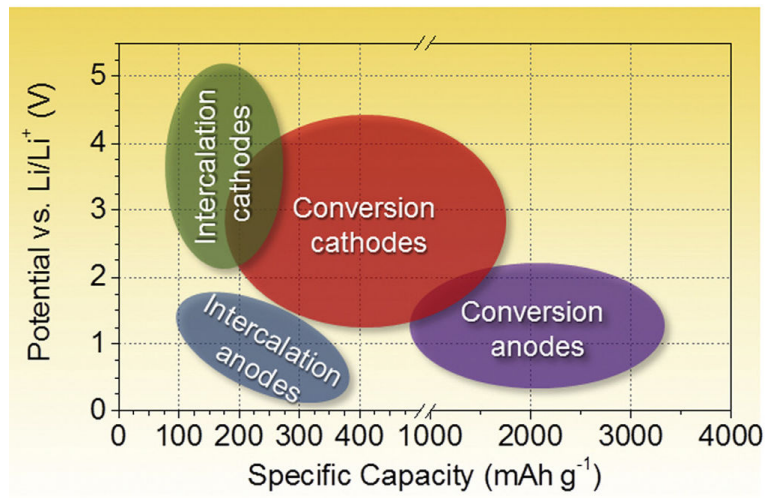


**Figure 1.1.1:** a) The theoretical capacity of graphite and various metal anodes. b) Reduction potential of various metal anodes. c) The elemental abundance in the crust.

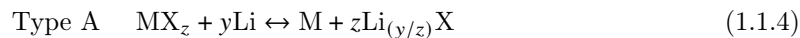
structural changes are mostly electrochemically reversible. Sulfides and organic materials mainly forms conversion type of cathodes.<sup>6, 17</sup>



17

**Figure 1.1.2:** an overview of the average discharge potentials and specific capacities for all types of electrodes.

The full reversible electrochemical reaction for conversion electrode materials is written as:



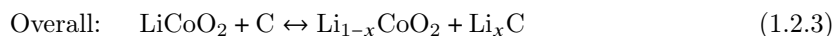
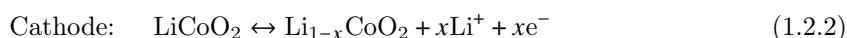
Type A category of cathodes ( Eq.1.1.4) includes metal halides comprising of high (2 or more) valence metal ions. S, Se, Te, and I follow the Type B reaction (Eq.1.1.5).

## 1.2. Lithium-ion Battery

A standard Li-ion cell uses a graphitic anode for intercalation,  $\text{LiCoO}_2$  layered intercalation cathode and  $\text{LiPF}_6$  in an ethylene carbonate/dimethyl carbonate as an electrolyte.<sup>19</sup> Since the  $\text{Li}^+$  ion has a low equivalent weight and a high redox potential (3.04 V vs. the normal hydrogen electrode (SHE)), research of lithium ion batteries with  $\text{Li}_x\text{TiS}_2$  layered materials started in the 1950s. These early cathode materials exhibited good reversibility and stability over a large range of x, but side reactions occurred at low voltages, limiting cell life.<sup>20</sup> Transition metal oxides make up the majority of new cathode materials for research and development in these batteries.

$\text{LiCoO}_2$  is a common cathode material, but  $\text{LiMn}_2\text{O}_4$  is used in certain applications that need a higher degree of protection.<sup>21</sup> The  $\text{LiCoO}_2$  (see fig.1.2.1) is common layered cathode materials among the  $\text{LiMO}_2$ (M = Co, Mn, Ni, Mg, Al, etc.) family. Lithium insertion takes place at octahedral sites between the framework of  $\text{CoO}_2$  sheets and forms  $\text{O}_3$  type layered structure.  $\text{Li}_x\text{CoO}_2$  provides 280  $\text{mAhg}^{-1}$  of theoretical capacity for complete delithiation.<sup>22</sup>

The electrochemical reactions with  $\text{LiCoO}_2$  as cathode material in a Li-ion battery can be written as:<sup>19</sup>



since the 1970's research efforts have been devoted in understanding and stabilizing the electrochemical performance of a wide variety of active materials for electrodes and electrolytes in rechargeable non-aqueous Li-ion batteries (see fig.1.2.2).<sup>21</sup>

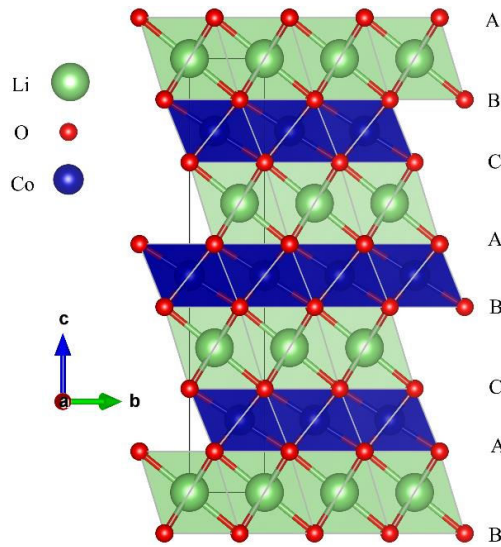


**Figure 1.2.1:** Rhombohedral structure of  $\text{LiCoO}_2$ . Co octahedra shown in blue, Li octahedra in green and the oxygen stacking is indicated by A, B and C.

| CATHODE   | ELECTROLYTE      | ANODE  |
|---|------------------|--|
| $\text{M}_x\text{O}_y$ ( $\text{M} = \text{V}, \text{Mn}$ )   | Organic Liquid   | Lithium Metal/Alloys   |
| $\text{MS}_2$ ( $\text{M} = \text{V}, \text{Ti}$ )  |                  |  |
| $\text{Li}_{1-x}\text{Co}_{1-y}\text{M}_y\text{O}_2$<br>( $\text{M} = \text{Ni}, \text{Mg}$ , etc)  | Ionic Liquid     | Lithiated Carbons  |
| $\text{Li}_{1-x}\text{Mn}_{1-y}\text{M}_y\text{O}_2$<br>( $\text{M} = \text{Co}, \text{Cr}$ , etc)  | Inorganic Liquid | Sn/Si-based Alloys   |
| $\text{Li}_{1-x}\text{Mn}_{2-y}\text{M}_y\text{O}_4$  | Inorganic Solid  | 3d-Metal Oxides  |
| Polyanion Compounds<br>$\text{Li}_x\text{MPO}_4$ ( $\text{M} = \text{Fe}, \text{Co}, \text{Mn}$ )<br>$\text{Li}_x\text{VOPO}_4, \text{LiVPO}_4\text{F}$ | Solid Polymer    | Metal Hydrides/Nitrides  |
| Organic Molecules<br>quinone $\text{Li}_4\text{C}_6\text{O}_6$  | Polymer Gel      | Organic molecules<br>Terephthalate $\text{Li}_2\text{C}_8\text{H}_4\text{O}_4$ |
|   | Hybrid System    |  |

**Figure 1.2.2:** List of representative electrode materials and electrolyte types investigated for rechargeable non-aqueous Li-ion batteries

In the following section we will discuss about the advantages and disadvantages of using Lithium-ion battery systems.

### **1.3. Advantages and limitations of using lithium ion batteries**

- Lithium ion batteries lead in most of the systems. Its smooth intercalation and high energy density results in long-term stability and fabrication in large scale power sources. Lithium batteries provide a longer life than lead-acid batteries and they still provide 80% of rated capacity after 2,000 cycles.<sup>23</sup>
- Lithium Ion batteries does not have memory effect like other batteries i.e. they do not need to be completely discharged. The self-discharge is less than half compared to nickel-cadmium batteries.<sup>24</sup>

Despite its overall advantages, these battery face some critical drawbacks as:

- It needs a protection circuit to maintain the safety. Its defective manufacture can result in bursting of these batteries. It also require to monitor the temperature extremes.
- Current state of the these cells have low energy density as compared to gasoline.
- Cathodes constitute almost 12% of total battery price and cobalt used in most of these batteries is more expensive than other transition metals.
- Cobalt and the electrolyte solvents being used are toxic and its dendrite formation can lead to short circuits.<sup>25</sup>

Further improvements in the energy density requires developing alternate chemistries, while maintaining the safety, power and lifetime of the existing LIBS

we will discuss the alternatives beyond LIBs in the following section.

### **1.4. Beyond lithium ion Batteries**

Existing Li-ion technology still has some potential for improvement. Instead, a paradigm shift is needed in the battery development process which includes materials-science breakthroughs, new electrode chemistries that can provide higher energy densities and new electrolytes that can deliver the high capacity. After the release of first commercial battery Li-ion battery by sony in 1991 huge research has been carried out to overcome the limitations discussed above. These technologies mainly focus on providing economical, sustainable as well as secure battery systems for large scale applications such as electric vehicles or grid storage. Several battery systems such as Mg-ion, Na-ion, Li-S and Li-Si batteries serve as the alternatives to Li-ion. Each of these alternatives face various obstacles which needs to be understood and overcome before bringing them in any commercial use.

### 1.4.1. Alloying compounds: Li-Si and Li-S

Graphite is the most exceptional of all Li-ion battery electrode materials. The only way to make an electrode with a higher energy density than graphite is to use materials with a higher specific/volumetric charge. At low potentials (< V vs Li<sup>+</sup>/Li) a variety of materials readily react with lithium via alloying or conversion mechanisms resulting in higher specific charge.<sup>26</sup> The term 'Alloying materials' refers to elements that electrochemically alloy with Li to form compound phases. Alloying materials may have exceptionally high volumetric and gravimetric capacities, but they are infamous for their massive volume expansion during lithiation. Si has earned the most attention of all alloying materials, because of its low average delithiation potential, (0.4 V vs. Li<sup>+</sup>/Li) with extremely high specific charge and volumetric charge density (3579mAh/g, 2190mAh/cm<sup>3</sup>perSi).<sup>27, 17</sup>

The alloying reaction with sulphur is another well-studied promising candidate. Sulphur is abundant, it forms Li<sub>2</sub>S on Li insertion resulting in high theoretical capacity of 1675 mAhg<sup>-1</sup>. Its low operating voltage (2.1 V vs. Li) and low density, on the other hand, result in low energy densities, while inherently low conductivity, its cell lifetimes and coulombic efficiency are limited by an 80% volume expansion and dissolution of intermediate reaction products.<sup>28</sup>

To resolve these challenges, a lot of research has been done. Sulphur encapsulation of carbon or polymers therefore reduces dissolution and reduces volume expansion. Producing carbon nanocomposites with Li<sub>2</sub>S improves conductivity. The electrolyte can also be adjusted to prevent polysulphide dissolution by inserting additives that form a stable SEI solid electrolyte interface (SEI) or using solid state electrolytes.<sup>29</sup>

### 1.4.2. Na-ion

In terms of electrochemical performance, sodium is the most straight forward alternative for lithium. The chemistry of both ions is highly similar i.e. the redox potential of sodium is somewhat close to that of lithium ( $E_{Na^+/Na} = -2.71$  V vs.  $E_{Li^+/Li} = -3.04$  V) both of them releases one electron while forming an ion, but sodium is three times heavier due to which sodium is unlikely to replace lithium in systems where total weight is a factor.<sup>30, 31</sup>

On the other hand because of its greater ionic radius, Na forms layered oxides of the P2-type structure, which are less susceptible to structural changes into spinel than its O3-type counterpart. Also Na and Al do not form alloys, therefore Al can be used as a current collector for both positive and negative electrodes. Lower cost and higher abundance makes sodium promising for large grid storage applications.<sup>32</sup>

| Ion              | Standard Electrode Potential (V) | Theoretical Capacity                     |                                  |   |
|------------------|----------------------------------|--|----------------------------------|---|
|                  |                                  | Specific Capacity (mAh g <sup>-1</sup> ) | Capacity (mAh cm <sup>-3</sup> ) | Volumetric Capacity (mAh cm <sup>-3</sup> ) |
| Li <sup>+</sup>  | -3.05                            | 3829                                     | 2044                             |   |
| Na <sup>+</sup>  | -2.71                            | 1165                                     | 1128                             |   |
| Mg <sup>2+</sup> | -2.36                            | 2234                                     | 3882                             |   |
| Ca <sup>2+</sup> | -2.87                            | 1337                                     | 2073                             |   |
| Zn <sup>2+</sup> | -0.76                            | 820                                      | 5854                             |   |
| Al <sup>3+</sup> | -1.66                            | 2980                                     | 8046                             |   |

**Table 1.4.1:** Comparison of univalent and multivalent standard electrode potentials and theoretical anode capacities

### 1.4.3. Multivalent working ions

The ability of the crystal structure to withstand ion insertion and removal, as well as the intrinsic redox properties, restrict electrochemical performance in lithium intercalation materials. Therefore, designing materials that can handle multiple ions, or electron transfers, could lead to a performance breakthrough. Multivalent cations, such as Mg<sup>2+</sup>, Ca<sup>2+</sup>, Zn<sup>2+</sup> and Al<sup>3+</sup> can transfer multiple electrons per ion. Therefore, in order to reach a given capacity, less ions are needed to be transported through the cell. This potentially offers a large increase in energy density over the monovalent Li-ion, or Na-ion technologies. When a single multivalent cation is inserted instead of several Li ions, the volume expansion is reduced, and thus structural stability is increased. In contrast to Li-ion cells, which include carbon anodes and copper current collectors, the option to use less reactive metals as anodes (Mg, Ca, Zn, or Al) reduces weight, volume, and cost. While the energy density of multivalent ions is expected to be greater, their redox potentials, and therefore predicted voltages, are lower than Li.(see Table. 1.4.1) .<sup>33 , 34</sup>

**Al-ion** Aluminum being the third richest element with lowest redox potential ( $E_{Al^{3+}/Al} = -1.66 \text{ V}$ ) involves three electrons, thereby providing a high charge-storage capacity. Its theoretical volumetric capacity is about four times higher than lithium and gravimetric capacity is comparable to that of Lithium. The most researched component for aluminum-ion batteries is the cathode.<sup>35</sup> The structural nature of graphitic carbons aids in the improvement of Al-ion battery efficiency. The cathode research in aluminum-ion batteries has received the most attention in which metal selenides are found to be an interesting cathode materials. Current Research of these batteries is lacking and the materials that have been studied have shown rapid capacity decay. Some systems are stable for >3000 cycles, and the material cost can be a determining factor on large scale.<sup>36 , 37 , 38</sup>

Aluminum, in general, is a viable lithium substitute for energy storage applications. Al-ion batteries have high rate capacities and aluminium is ten times less expensive than lithium.

Increasing number of research papers are being published in the area of multivalent Electrochemistry as seen from Fig.1.4.1<sup>39</sup>

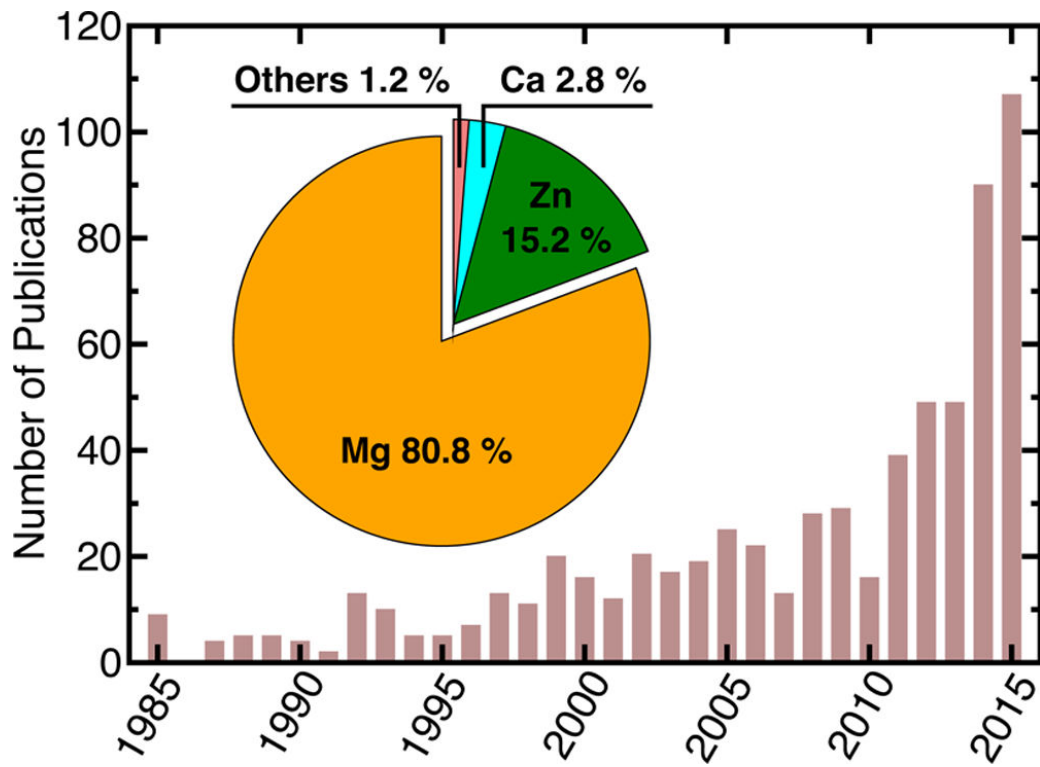


**Figure 1.4.1:** Number of publications from 1985 until 2015 featuring multivalent electrochemistry. The pie chart corresponds to the distribution of this research for different chemistries (Mg, Zn, Ca, etc.)

It can be seen that Mg-ion battery has attracted the most attention among the numerous reversible electrochemistries. Our work also mainly focuses on Magnesium ion battery. In the following section we'll go over the reasons why Mg-ion is such a unique candidate.

## Chapter 2

# Rechargeable Magnesium Battery

Magnesium-ion technology is exciting for many factors, Magnesium has superior properties compared to lithium. It is a low-cost substance and one of the most abundant element (about 2.3 wt % of the earth's crust). With a density of  $1.74 \text{ gcm}^{-3}$ , Magnesium is one of the lightest structural metals in the earth's crust and is intended to minimise the average weight of energy storage systems.<sup>40</sup> <sup>9</sup> The divalent nature of magnesium with low reduction potential among multi-valent ions (see Table 1.4.1) and second behind lithium results in a high theoretical volumetric capacity of  $3833 \text{ mAhcm}^{-3}$ (see fig 2.0.2b).<sup>41</sup> <sup>42</sup> Mg anodes, in contrast to alkali metal (Li, Na, and K) anodes, appear to form a smooth and homogeneous deposition layer during electrodeposition, preventing dendrite nucleation thus making them safer for commercial use.<sup>43</sup> In 2000, Aurbach et al.<sup>44</sup> made a revolution in MIB science by suggesting the first MIB prototype method, which consisted of a Chevrel phase cathode ( $\text{Mo}_6\text{S}_8$ ), a Mg anode, and an organohaloaluminate salt as an electrolyte solution. It showed impressive cycling capacity for more than 2000 cycles.<sup>44</sup> Since then, a great deal of research has been carried out on MIBs. (see fig. 2.0.1)<sup>6</sup>

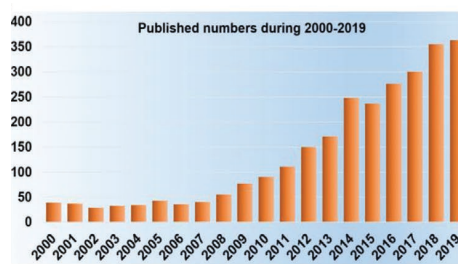


**Figure 2.0.1:** The number of published papers related to magnesium batteries

MIBs function in a similar way to LIBs in that they depend on the reversible intercalation and deintercalation of magnesium ions on the cathode and anode.(see fig.2.0.2a)<sup>5</sup>

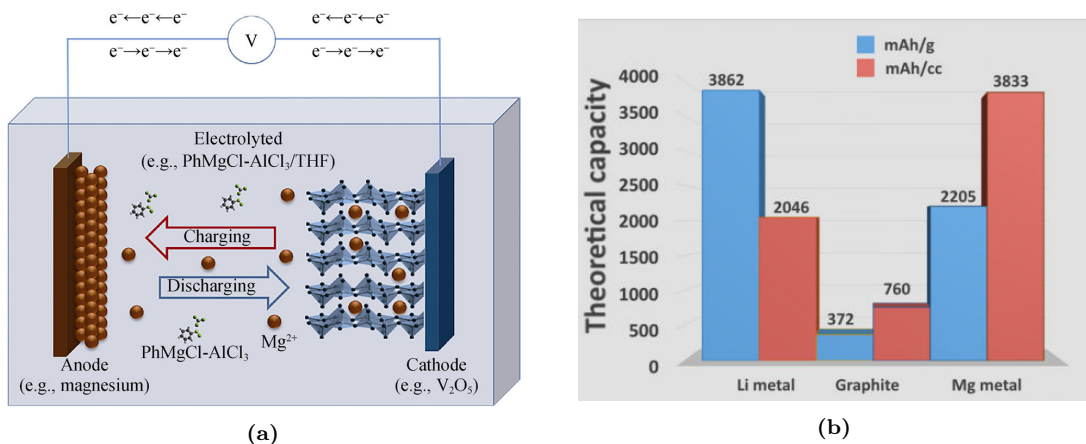


**Figure 2.0.2:** (a)Schematic diagram of typical electrochemical reaction process of MIBs with (Mg as anode,  $V_2O_5$  as cathode,  $PhMgCl - AlCl_3/THF$  solution as electrolytes) (b)Theoretical capacity comparison between Li, graphite and Mg

Despite these advantages, magnesium-ion technology has lagged behind lithium-ion technology in terms of advancement. One of the challenges is the development of a good electrolyte which has been a major stumbling block. The surface of the Mg metal electrode produces a passivation layer in most traditional polar aprotic solvents containing simple salt anions such as ( $ClO_4^-$ ,  $PF_6^-$ ,  $BF_4^-$  etc.), which prevents the reversible deposition of  $Mg^{2+}$  ions, resulting in low coulombic efficiency.<sup>45</sup> Another significant obstacle is the manufacture of cathode materials with high reversible capacity and sufficient operating voltage. Due to the unique divalent character of  $Mg^{2+}$  causes large polarization and strong solvation of  $Mg^{2+}$ , resulting in sluggish kinetics of solid state diffusion through inorganic cathode materials.<sup>46</sup> ,<sup>47</sup> To address these issues, several strategies have been reported. In the following section we will overview recent research progress on electrode materials of RMBs

## 2.1. Recent advances in Electrolytes and Anodes

One of the major benefits of using magnesium as the working ion is that unlike alkali metals lower reactivity of Magnesium allows it to be used as an anode directly, and Mg metal forms a smooth and uniform deposition layer easily during the charging. It is important to develop an anode that can effectively avoid passivation layer formation and improve the kinetics of magnesium. The materials used for the anode of RMBs are mainly modified Mg metal anodes<sup>48</sup> , alloy-based materials<sup>49</sup> , carbon-based materials etc.

As discussed earlier Mg metal anode reacts with most conventional electrolytes forms non-conductive

$Mg^{2+}$  passivation layer unlike the case of  $Li^+$  ions where the films are good ionic conductor. This incompatibility has led to investigation of several Electrolyte alternatives. Among the Liquid Electrolytes Grignard-Based Electrolytes performed well in RMBs. The Grignard reagent  $R\text{MgX}$  ( $R$  can be alkyl or aryl;  $X$  can be Cl, Br, or other halides) produces a passivation-free Mg surface and allows for reversible Mg deposition–dissolution with high coulombic efficiency.<sup>50</sup> Further adding ionic liquid additives have also been reported in enhancing anodic stability and ionic conductivity of Grignard based electrolytes.<sup>51</sup> Many solid-state RMB researches have been inspired by solid-state LIBs which includes inorganic solid-state electrolytes, organic solid-state electrolytes, and organic-inorganic composite solid-state electrolytes. Organic solid-state electrolytes also called solid-state polymer electrolytes is the most promising candidate among them. Apart from high ionic conductivity, polymer-based solid electrolytes have excellent electrochemical performance without causing internal short circuit,electrolyte leakage and have high electrochemical and thermal stabilities.<sup>52</sup>

## 2.2. Cathodes

The cathode material is one of the most important components of RMBs. The perfect cathode material has the following properties i) high operating voltage and specific capacity ii) rapid and reversible  $Mg^{2+}$  ion migration kinetics iii) strong cycling stability. The motivation for concentrating on novel Mg-ion cathodes is that those that have been reported so far have been restricted to capacities of less than  $200 \text{ mAhg}^{-1}$  over a limited number of cycles and voltages of less than 2.0 V vs. Mg, making them incompatible with Li-ion technologies. The following sections gives a short review of suggested intercalation cathode materials for RMBs.

### 2.2.1. Molybdenum sulfide

#### Chevrel phase: $\text{Mo}_6\text{T}_8$ where $\text{T} = \text{S}$ or $\text{Se}$

For RMBs, the Chevrel phase was the first and most successful intercalation cathode material.<sup>53</sup> CP-based cathode have energy storage capability comparable to LIBs, it also acts as a benchmark for evaluating the electrochemical behaviour of newly formed magnesium electrolytes and membranes. The Chevrel phase can be seen(see fig.2.2.1) as the stacking of  $\text{Mo}_6\text{S}_8$  blocks. Inside a cube of 8 sulphur atoms 6 molybdenum atoms form an octahedron  $\text{S}_8$  anions reside in the corners and octahedron.<sup>50</sup>

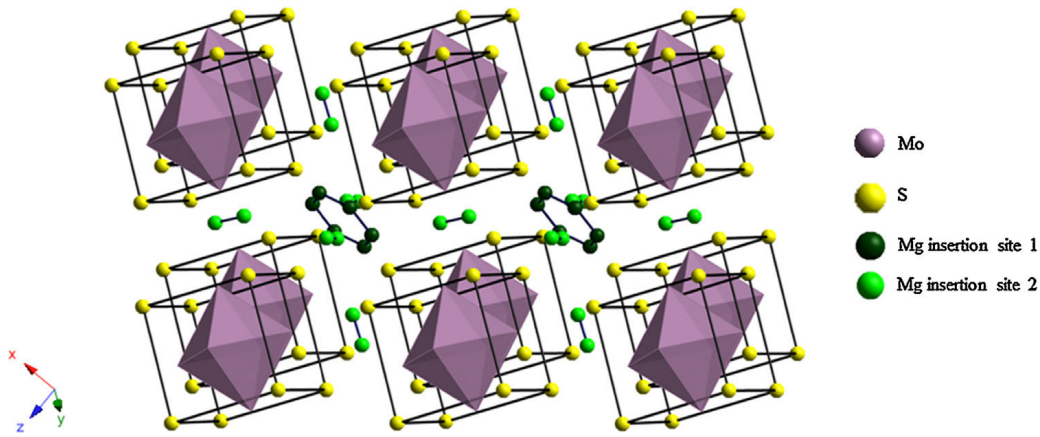


**Figure 2.2.1:** Chevrel Phase  $\text{Mo}_6\text{S}_8$  crystallographic structure

Magnesium insertion into  $\text{Mo}_6\text{S}_8$  first occupies the ring arrangement (see fig. 2.2.2a) in insertion site 1 which has a lower potential energy than insertion site 2. Intercalation into site 1 involves the first transfer of 2 electrons to create  $\text{MgMo}_6\text{S}_8$ . Inner-ring diffusion is much faster than the outer-ring diffusion.<sup>5</sup>

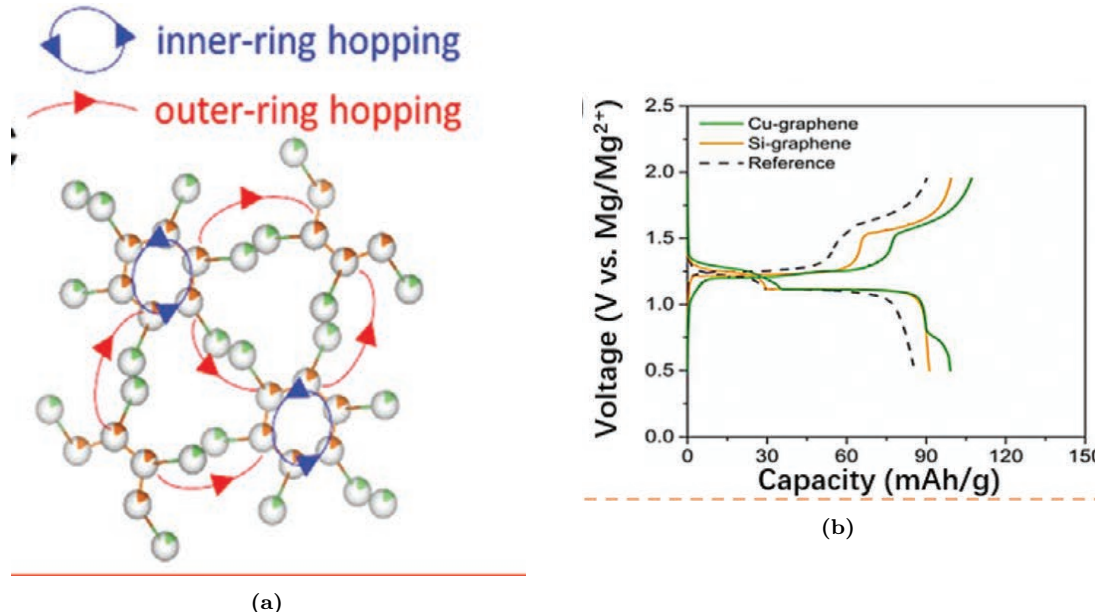
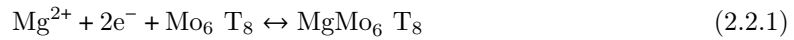


**Figure 2.2.2:** a) Inner-ring and outer-ring hopping between partially occupied outer and inner sites  
b) Charge/discharge curves and cycle performance of  $\text{Mo}_6\text{S}_8$  cathode containing different materials

Generally, the intercalation of Mg<sup>2+</sup> is done in two steps as:<sup>54, 55</sup>



The excellent cyclability of Mo<sub>6</sub>S<sub>8</sub> was the most exciting feature. The Chevrel Phase could be cycled over 2000 times at 100% depth of discharge with less than 15% capacity fading. However, one main disadvantages of Mo<sub>6</sub>S<sub>8</sub> is its poor intercalation/deintercalation voltage (1.1 V vs Mg<sup>2+</sup>/Mg), which would certainly reduce the output energy density.<sup>56</sup> Methods to increase performance of the Mo<sub>6</sub>S<sub>8</sub> cathode have been attempted repeatedly. Reducing the particle size of Mo<sub>6</sub>S<sub>8</sub> clusters at nanoscale is an effective method. Because of the smaller particle size results in the shorter Mg<sup>2+</sup> diffusion path and the faster kinetics within the particles.<sup>57</sup> Cu<sub>x</sub>Mo<sub>6</sub>S<sub>8</sub>, the precursor of Mo<sub>6</sub>S<sub>8</sub> has also been shown to have excellent Mg<sup>2+</sup> (de)intercalation performance. The presence of elemental Cu in the ternary Cu<sub>x</sub>Mo<sub>6</sub>S<sub>8</sub> structure makes it free of charge trapping during cycling, which has a positive effect on the performance of RMBs. Charge trapping in first site can be reduced by substituting selenium for sulfur. The Substitution create a triclinic distortion to the crystal structure which lower the activation barrier (see fig.2.2.2b).<sup>58</sup>

Other intercalation materials with higher voltage and charge storage capacity are encouraged to be discovered.

### 2.2.2. Layered Structure Cathode Materials

Layered structure materials have significant importance as electrode materials. Like in the case of Li-ion Layered materials are also promising for Mg<sup>2+</sup>intercalation due to their poor van der Waals force. Their unique 2D properties provides large number of chemical activity sites as well as fast ion insertion/extraction. Among them layered transitional metal oxides have been considered as one of the most promising cathode candidates for RMBs interms of high working voltage, low cost, and structural stability.<sup>59</sup> In the following section we will discuss some representative transition metal oxides such as V<sub>2</sub>O<sub>5</sub>, MoO<sub>3</sub>

#### V<sub>2</sub>O<sub>5</sub>

The layered oxide V<sub>2</sub>O<sub>5</sub> has received special interest and has showed a good reversible capacity at high voltage (up to 250 mAhg<sup>-1</sup> at 3.0 V vs. Mg). The layered structure consists of both edge and corner sharing VO<sub>5</sub> square pyramids with a corner sharing tetrahedral cation insertion site consists of layered V<sub>2</sub>O<sub>5</sub> polyhedral matrix structure, the crystal structure is depicted in Fig.2.2.3a Since four coordinate sites are not favoured, a tetrahedral site can be advantageous for Mg<sup>2+</sup> diffusion. As a result, diffusion barriers are lower than when occupying octahedral sites.<sup>60</sup> V<sub>2</sub>O<sub>5</sub> exists in

mainly the  $\alpha$  and the  $\delta$  polymorphs.  $V_2O_5$  undergoes a structural transformation from  $\alpha$ - $V_2O_5$  to  $\delta$ - $Mg \cdot 5V_2O_5$  and  $\gamma$ - $MgV_2O_5$

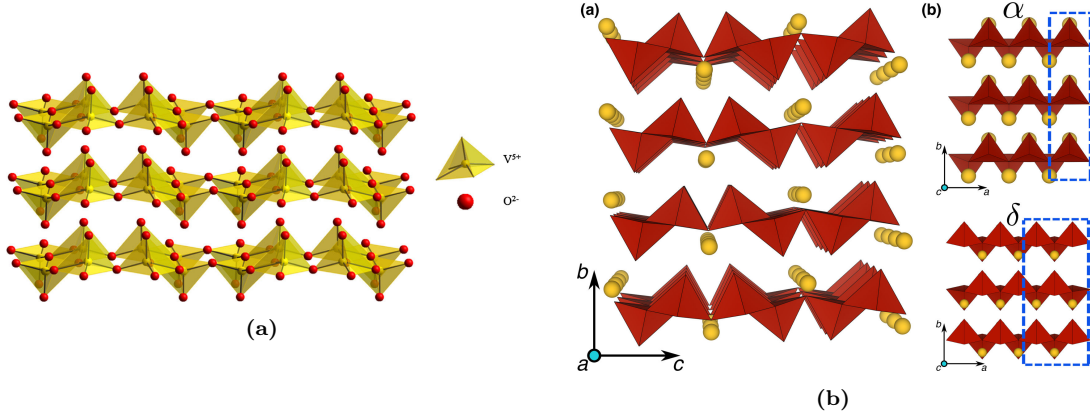


**Figure 2.2.3:** a)Crystallographic structure of crystalline  $VO_5$  where Red pyramids indicate  $VO_5$  polyhedra and the yellow atoms are intercalants b)Different polymorphs of  $V_2O_5$ . materials

Nov'ak et al.<sup>61</sup> first reported that a layered  $V_2O_5$  structure enabled the insertion of  $Mg^{2+}$  at room temperature. The highest coulombic capacity of  $V_2O_5$  was discovered to be up to  $170Ahkg^{-1}$  in the initial testing. But it had only 20 cycles and the capacity attenuation was very fast. The reason for the same may be the slow Intercalation of  $Mg^{2+}$  possibly due crystal phase transitions. Despite of high open circuit voltage, the use of  $V_2O_5$  is limited due to its poor electrical conductivity and unstable structure. In this view several recent studies have proposed strong reactivity of  $Mg^{2+}$  ions with various morphologies of  $V_2O_5$ , such as  $V_2O_5$  nanotubes (NTs),  $V_2O_5$  gel, and  $V_2O_5$ /carbon composites.

Diffusion path length within  $V_2O_5$  crystals gets reduced as crystallite size reduces, this improves the capacity at higher current rates. This approach has been used in work on nanocrystalline  $V_2O_5$  and  $V_2O_5$  nanotubes. In addition, the cycling performance of  $VO_x$ -NTs can be also improved by using  $Mg(ClO_4)_2$ -based electrolytes in tetramethylsilane ethyl acetate (TMS-EA) mixed solvents.<sup>62</sup> The  $V_2O_5$  xerogel has low crystallinity and a longer interlayer distance. The coordination of water in the electrolyte and the structured water in xerogel- $V_2O_5$  improves the performance of  $V_2O_5$ . The water content in the cathode is proved to be essential for shielding the  $2^+$  charge of magnesium ions to facilitate the intercalation.<sup>63</sup>

### **MoO<sub>3</sub>**

$MoO_3$  is another known layered oxide cathode material for RMBs. The double layers consist of edge and corner-sharing  $MoO_6$  octahedron(fig.2.2.4), and these layers are connected by weak van

der Waals attraction forces, which promote the insertion and extraction of  $Mg^{2+}$ . With high-purity thin-film  $MoO_3$  as the cathode, a reversible Mg capacity of  $220\text{mAhg}^{-1}$  at  $>95\%$  efficiency is obtained in  $0.1\text{ m MgTFSI}_2/\text{AN}$  solutions. Furthermore, with the increase of water concentration in the solutions, the specific capacity of the  $\alpha-\text{MnO}_2$  cathodes increases significantly.<sup>64</sup>

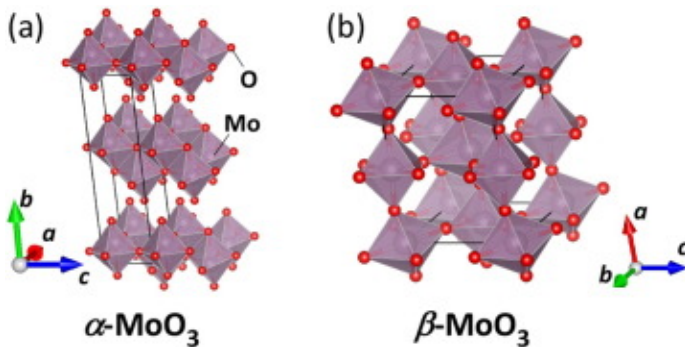


**Figure 2.2.4:** The crystal structures of  $MnO_3$

### 2.2.3. Spinel Structure Cathode Materials

The spinel structure demonstrates the general formula of  $MgT_2X_4$  with the space group  $Fd\bar{3}m$ , where the octahedral cation ( $T$ ) in the packed lattice is coordinated by the cubic anion ( $X$ ). Such an edge-sharing configuration gives rise to 3D diffusion paths. Spinel compounds have advantages such as, high capacity and working voltage, which are promising to increase the energy density of RMBs. However, the  $Mg^{2+}$  diffusion energy barrier is quite high and therefore, is unfavorable for reversible  $Mg^{2+}$  intercalation. To tackle these issues Sinha and Munichandraiah.<sup>65</sup> first reported a spinel-like  $MgMnO_4$ . After 20 cycles, the cathode material had a specific capacity of  $42\text{ mAhg}^{-1}$  and stabilised at  $35\text{ mAhg}^{-1}$ ,  $\lambda-\text{MnO}_2$  is also demonstrated as cathode materials for  $Mg^{2+}$  intercalation. Phase transformation of  $\lambda-\text{MnO}_2$  into spinel-like  $MgMn_2O_4$  is likely to affect the mobility of  $Mg^{2+}$  in spinel-structured materials.<sup>66</sup> The high initial capacity, cycling properties and compatibility in water based electrolytes make  $\lambda-\text{MnO}_2$  worthy of future research. Several research groups have also looked at spinel transition metal sulphides materials, which have a higher  $Mg^{2+}$  mobility than their oxide equivalents, therefore allows the better electrochemical efficiency.

### 2.2.4. Polyanionic Compounds

Polyanionic compounds with 3D network structures consist of transition metals and polyanions with strong covalent bonds. These materials have several advantages like high voltage and stability. Their instability at deep charge and after many cycles limits their practical capacity. Among these structure Olivine-type  $MgMSiO_4$  ( $M = Fe, Mn, Co, or Ni$ ) possesses a high theoretical capacity and

high theoretical redox potential. The structural stabilities and multi-valent transition metal cores of these materials allow for reversible magnesium ion insertion without much structural damage or magnesium ion trapping. The transition metal first reduces from  $4^+$  to  $3^+$  and then from  $3^+$  to  $2^+$  which correlates with the two CV peaks. Crystal reordering may shorten the life cycle of this material by causing structural damage.<sup>67</sup>

# Chapter 3

## Theoretical Background

### 3.1. Introduction to density functional theory

The aim of *ab initio* methods is to solve the Schrödinger equation or a similar quantum mechanical equation appropriate potential. The Schrödinger equation solutions describe a system's quantum state, which contains the information from which other physical properties of the system can be deduced. In general, solving the Schrödinger equation precisely for structures of more than an electron is incredibly complicated. As a result, over time, different estimated approaches have been suggested and developed, each with its own set of advantages and drawbacks.

Wave function-based and density-functional-based models are often used to classify these processes. Many wave function-based methods (such as quantum chemical approaches, quantum Monte Carlo, and so on) are also more precise than density-functional theory-based methods (DFT). Coupled cluster, in particular, is often regarded as the theoretical gold standard and is often used as a benchmark. Unfortunately, also with the world's biggest computers and most powerful algorithms, the computing cost of coupled cluster and other wave function based methods increases dramatically with size of system, and handling only a few tens of electrons becomes a bottleneck. In this respect DFT has emerged as a very useful technique, because, it is capable of dealing with systems with hundreds or thousands or even more electrons.

Undoubtedly, DFT is the most popular *ab initio* method nowadays, especially for condensed phase simulations. Since the first DFT simulation of liquid water was performed in 1993<sup>68</sup>, DFT has continued to bring new insights to various properties of liquid water, ice, interfacial water, confined water, solvation, adsorbed water , proton transfer, etc. However, compared with all electronic structure methods, DFT has some shortcomings. These shortcomings are mostly concerned with

accuracy. DFT is exact in principle, but in practice, it requires an approximation for the treatment of the so called electron exchange and correlation interactions.

The exchange-correlation (xc) energy makes up a small part of a system's overall energy. This, on the other hand, turned out to be extremely important for accurately describing atomic binding. Two standard ways are proposed to calculate the xc energy and are the local-density approximation (LDA) and the generalized gradient approximation (GGA<sup>69</sup>). These two xc-functionals have been extremely successful in various fields. But they often fail for the treatment of weakly bound systems (e.g., hybrid systems and van der Waals bond). For purely van der Waals (vdW) bonded systems both LDA and GGA are known to be inadequate. However, for H-bonded systems or mixed H-bonded and vdW bonded systems it is somewhat unclear how these functionals perform. There are more sophisticated xc functionals than LDA and GGA are also reported in recent years. But, how these functionals perform and how they systematically improve the performance of DFT xc-functional for weakly bonded systems remain open questions.

### 3.1.1. Electronic Structure Problem

A key aim of most electronic structure theory is to solve the non-relativistic time independent Many-body Schrödinger equation

$$\hat{H}\Psi(\{R_A\}, \{r_i, \sigma_i\}) = E\Psi(\{R_A\}, \{r_i, \sigma_i\}) \quad (3.1.1)$$

For a system containing M nuclei and N electrons the many-body wave function ( $\Psi$ ) is a function of all the spatial coordinates of nuclei ( $\{\mathbf{R}_A\}, A = 1, \dots, M$ ). The Hamiltonian ( $H$ ) is a sum of all possible interactions between electrons and nuclei. In atomic units (energy in Hartree and length in Bohr),  $\hat{H}$  can be expanded as:

$$\hat{H} = - \sum_{i=0}^N \frac{\nabla_i^2}{2} - \sum_{A=1}^M \frac{\nabla_A^2}{2M_A} + \sum_{i=1}^N \sum_{j>i}^N \frac{1}{|r_i - r_j|} + \sum_{A=1}^M \sum_{B>A}^M \frac{Z_A Z_B}{|R_A - R_B|} - \sum_{i=1}^N \sum_{A=1}^M \frac{Z_A}{|r_i - R_A|} \quad (3.1.2)$$

In the above equation,  $M_A$  is the ratio of the mass of nucleus  $A$  to the mass of an electron and  $Z_A$  is the atomic number of nucleus  $A$ . The  $\nabla_i^2$  and  $\nabla_A^2$  are the Laplacian operators. The first two terms in Eqn.(3.1.2) represent the kinetic energies of all the electrons and nuclei, respectively. The third and fourth term, respectively, correspond to the Coulomb repulsion between electrons and between nuclei. The fifth term is the Coulomb attraction between electrons and nuclei. Though the Eqn.(3.1.1) is deceptively simple by its form it is enormously complex to solve. Ever since it was discovered it is a dream for researchers to find reasonable approximations to reduce the complexity. The first important approximation is obtained by decoupling the dynamics of the electrons and the nuclei, which is known as Born-Oppenheimer approximation.

### 3.1.2. Born-Oppenheimer Approximation

The very essence of the Born-Oppenheimer approximation comes from the fact that the nuclei are much heavier than the electrons. Even for the lightest nucleus, a proton, its mass is approximately 2000 times larger than the electrons. So, in most cases the timescale of the response of the electrons is a few orders of magnitude faster than that of the nuclei, which allows the dynamics of the electrons and nuclei to be decoupled. Through this simple approximation, nuclei can be treated as classical particles and can be considered as static with respect to quantum particle electrons. Then for any given nuclear configurations the electrons are assumed to remain in their instantaneous ground state. As a result, the second term in Eqn.(3.1.2) can be neglected and the fourth term i.e. the repulsion between nuclei can be treated as a constant for a fixed configuration of the nuclei. The remaining terms in Eqn. (3.1.2) are called the electronic Hamiltonian ( $\hat{H}_e$ ),

$$\hat{H}_e = - \sum_{i=1}^N \frac{\nabla_i^2}{2} + \sum_{i=1}^N \sum_{j>i}^N \frac{1}{|\mathbf{r}_i - \mathbf{r}_j|} - \sum_{i=1}^N \sum_{A=1}^M \frac{Z_A}{|\mathbf{r}_i - \mathbf{R}_A|}. \quad (3.1.3)$$

The solution to a Schrödinger equation involving the electronic Hamiltonian ( $\hat{H}_e$ ) becomes

$$\hat{H}_e \Psi_e(\{\mathbf{R}_A\}, \{\mathbf{r}_i, \sigma_i\}) = E_e \Psi_e(\{\mathbf{R}_A\}, \{\mathbf{r}_i, \sigma_i\}). \quad (3.1.4)$$

The electronic wave function ( $\Psi_e$ ) depends on nuclear coordinates ( $\{\mathbf{R}_A\}$ ) only parametrically now, thus for fixed configuration of nuclei we suppress  $\{\mathbf{R}_A\}$ . Furthermore, for simplicity we put together electronic spatial and spin coordinates ( $\{\mathbf{r}_i \sigma_i\}$ ) into one variable  $\{\mathbf{x}_i\}$  (i.e.,  $\{\mathbf{x}_i\} = \{\mathbf{r}_i \sigma_i\}$ ) and rewrite Eq. as  $\hat{H}_e \Psi_e(\{\mathbf{x}_i\}) = E_e \Psi_e(\{\mathbf{x}_i\})$ . The total energy for some fixed configurations of the nuclei will also include the constant nuclear repulsion term leading to,

$$E_{total} = E_e + \sum_{A=1}^M \sum_{B>A}^M \frac{Z_A Z_B}{|\mathbf{R}_A - \mathbf{R}_B|} \quad (3.1.5)$$

In general, under the Born-Oppenheimer approximation, the electronic structure problem reduces to solving Eqn 3.1.5 and from that the total energy of the system can be obtained. However, one should bear in mind that the Born-Oppenheimer approximation is certainly not universally valid. It is well known that the Born-Oppenheimer approximation will break down when there are multiple potential energy surfaces close to each other in energy or crossing each other. Dissociative adsorption of molecules on metal surfaces is a famous contemporary example. Similarly, reactions involving hydrogen and proton transfer may be susceptible to breakdowns in the Born-Oppenheimer approximation.

The major difficulty in solving Schrödinger equation is the interaction between electrons, where all

the many-body quantum effects are hidden. Since the motion of the electrons is correlated, one should know the instantaneous coordinates of each electron, which essentially requires the treatment of  $3N$  variables for an  $N$ -electron system. Despite the almost intractable nature of these interactions, many approximate methods have been developed to solve Schrödinger or Schrödinger-like equations by mapping the  $N$ -electron Schrödinger equation into effective one-electron Schrödinger-like equations, which are easier to tackle.

The different approximate schemes employed here can be divided into two major categories:

1. The wave function based methods, where the many-electron wave function is the key.
2. Density functional theory, in which electron density is the central quantity.

Here, the wave function based methods will be introduced first.

### 3.1.3. Wave Function Based Methods

As mentioned above, the fundamental quantity for the wave function based methods is the many electron wave function,  $\Psi$ , whose correct functional form is far from simple. The first step in the determination of  $\Psi$  is often simply an educated guess and then reliance on the variational principle. The variational principle tells that the expectation value of the electronic Hamiltonian ( $\hat{H}_e$ ) for any guessed or trial wave function is always larger (upper bound) than the electronic ground state energy  $E_0[\Psi_0]$  and the equality will hold only when the wavefunction is in the true ground state ( $\Psi_0$ ), *i.e.*,  $(E[\Psi] \geq E_0[\Psi_0])$ . The advantage of the variational principle is that starting with a trial wave function one can approach towards the ground state energy  $E_0[\Psi_0]$  by variationally improving the quality of the wave function. In the following, the variational principle will be applied to minimize the approximated Hartree-Fock wave function.

#### The Hartree-Fock Approximation

The Hartree-Fock (HF) approach is regarded as the fundamental first step in much of quantum world. In the HF approach the wave function of interacting  $N$ -electrons,  $\Psi(\{\mathbf{x}_i\})$ , can be approximately described with a single Slater determinant. A Slater determinant is nothing but a linear combination of the product of independent electron wave functions ( $\{\phi_i(\mathbf{x}_i)\}$ ) (also known as spin orbitals) with all possible combinations of the permutations of their coordinates. Also, the Slater determinant satisfies the antisymmetric property of the electronic wave function, which is essential because electrons are fermions and obey Pauli's exclusion principle. For an  $N$ -electron system the HF wave function looks like

$$\Psi(\{\mathbf{x}_i\}) \approx \Psi^{HF}(\{\mathbf{x}_i\}) = \frac{1}{\sqrt{N!}} \begin{vmatrix} \varphi_i(x_i) & \varphi_j(x_i) & \dots & \varphi_N(x_i) \\ \varphi_i(x_j) & \varphi_j(x_j) & \dots & \varphi_N(x_j) \\ \vdots & \vdots & \ddots & \vdots \\ \vdots & \vdots & \ddots & \vdots \\ \varphi_i(x_N) & \varphi_j(x_N) & \dots & \varphi_N(x_N) \end{vmatrix}$$

In the Slater determinant each of the columns are labeled by spin orbitals and exchange of two electron coordinates will interchange the two columns inside the determinant, thus satisfying the antisymmetric requirement. The antisymmetric property of the Slater determinant can be simply realized considering a two-electron system:

$$\Psi(x_1, x_2) = \frac{1}{\sqrt{2!}} [\varphi_1(x_1) \varphi_2(x_2) - \varphi_2(x_1) \varphi_1(x_2)] = -\Psi(x_2, x_1). \quad (3.1.6)$$

Now using the HF wave function the electronic energy can be written as,

$$\begin{aligned} E^{HF} &= \langle \Psi^{HF} | \hat{H}_e | \Psi^{HF} \rangle \\ &= \sum_{i=1}^N \int \varphi_i^*(x_i) \left[ -\frac{\nabla_i^2}{2} + V^{ext}(x_i) \right] \varphi_i(x_i) dx_i \\ &\quad + \frac{1}{2} \sum_{i=1}^N \sum_{j=1}^N \iint \varphi_i^*(x_i) \varphi_j^*(x_j) \frac{1}{|r_i - r_j|} \varphi_j(x_j) \varphi_i(x_i) dx_i dx_j \\ &\quad - \frac{1}{2} \sum_{i=1}^N \sum_{j=1}^N \iint \varphi_i^*(x_i) \varphi_j^*(x_j) \frac{1}{|r_i - r_j|} \varphi_j(x_i) \varphi_i(x_j) dx_i dx_j. \end{aligned} \quad (3.1.7)$$

The above equation can be treated as an energy functional,  $E^{HF}[\{\varphi_i^*(x_i)\}, \{\varphi_i(x_i)\}]$ , and can be minimized variationally by applying Lagrange undetermined multiplier subject to the constraints that the independent electron wave function  $\{\phi_i(\mathbf{x}_i)\}$  are orthonormal, *i.e.*,  $\langle \phi_i(\mathbf{x}_i) / \phi_j(\mathbf{x}_j) \rangle = \delta_{ij}$ . This leads to a mapping from a complex  $N$ -electron Schrödinger equation in to effective one electron Schrödinger -like equation

$$\hat{H}_i \varphi_i(x_i) = \epsilon_i \varphi_i(x_i), \hat{H}_i = -\frac{\nabla^2}{2} + V^{ext}(x_i) + V^{Hartree}(x_i) + V_i^{Exchange}(x_i). \quad (3.1.8)$$

$\hat{H}_i$  represents a one-electron Hamiltonian, known as the Fock operator. The variables  $\epsilon_i$  and  $\phi_i$  are the corresponding eigenvalues and eigenvectors, respectively. The first two terms in  $\hat{H}_i$  are, respectively, the kinetic energy of  $N$  independent electron and the external potential. The external potential,  $V^{ext}(\mathbf{x}_i)$ , is the Coulomb attraction on  $i^{th}$  electron due to all the nuclei. The

third and fourth terms approximately account for the many body electron – electron interactions.  $V^{Hartree}(\mathbf{x}_i)$  is the Hartree potential, which is the Coulomb repulsion between  $i^{th}$  electron and the electron density produced by all electrons and can be defined as  $V^{Hartree}(\mathbf{x}_i) = \int \frac{n(x_j)}{|r_i - r_j|} dx_j$ ,  $n(x_j) = \sum_{j=1}^N |\varphi_j(x_j)|^2$ . The fourth term solely appears from the antisymmetric nature of the wave function and is known as *exchange* potential ( $V_i^{Exchange}(\mathbf{x}_i)$ ). Unlike  $V^{ext}(\mathbf{x}_i)$  and  $V^{Hartree}(\mathbf{x}_i)$ ,  $V_i^{Exchange}(\mathbf{x}_i)$  does not have any classical analogy and it can only be written as an integral operator

$$V_i^{Exchange}(x_i)\varphi_i(x_i) = [\sum_{j=1}^N \int \varphi_j^*(x_j) \frac{1}{|r_i - r_j|} \varphi_j(x_i) dx_j] \varphi_i(x_j). \quad (3.1.9)$$

As evident from the above equation,  $V_i^{Exchange}(\mathbf{x}_i)$  leads to an exchange of the variable in the two spin orbitals. Furthermore, the exchange operator,  $V_i^{Exchange}(\mathbf{x}_i)$  is said to be a nonlocal operator. As the results of  $V_i^{Exchange}(\mathbf{x}_i)$  operating on the spin orbital,  $\phi_i(\mathbf{x}_i)$  will depend on the value of  $\phi_i(\mathbf{x}_i)$  throughout all space. It is worth to mention that, when  $i=j$ , the last two terms in Eq.3.1.9 cancel each other and so by construction the HF method is self-interaction free. Eq. 3.1.9 is the usual form of the HF equation, which is a linear eigenvalue problem and must be solved self consistently. The HF method treats the exchange interaction between electrons with the same spin exactly and often in the literature it is described as an *exact exchange* approach. The HF method is used extensively to study various materials science problems, such as adsorption, defects in solids, and electronic structure of insulators.

### 3.1.4. Density-Functional Theory

Density-functional theory differs from the wave function based methods by using the electron density  $n(\mathbf{r})$  as the central quantity. An important advantage of using the electron density over the wave function is the much reduced dimensionality. Regardless of how many electrons one has in the system, the density is always 3 dimensional. This enables DFT to readily be applied to much larger systems, i.e. hundreds or even thousands of atoms become possible. Partly, for this reason, DFT has become the most widely used electronic structure approach today, particularly in the condensed matter physics community. In this section, a basic introduction to DFT will be given. Authoritative and comprehensive discussions of DFT can be found in a range of excellent review article<sup>69</sup> and textbooks.<sup>70</sup>

First, the electron density is defined as,

$$n(\mathbf{r}) = N \int \dots \int |\Psi(x_1, x_2, \dots, x_N)|^2 d\sigma_1 dx_2 \dots dx_N \quad (3.1.10)$$

where  $\{\mathbf{x}_i\}$  represents both spatial and spin coordinates. The electron density  $n(\mathbf{r})$  determines

the probability of finding any of the  $N$  electrons within the volume, but with arbitrary spin while the other  $N-1$  electrons have arbitrary positions and spin in the state represented by  $\Psi$ . This is a non-negative simple function of three variables,  $x$ ,  $y$ , and  $z$ , integrating to the total number of electrons,  $N = \int n(\mathbf{r}) d\mathbf{r}$ .

### Thomas-Fermi Model

The proposition of electronic energy can be expressed in terms of the electron density was first exploited back in 1920s by Thomas and Fermi<sup>[71;72](#)</sup>. In Thomas-Fermi model, the kinetic energy of the electrons is derived from the quantum statistical theory based on the uniform electron gas, but the electron–nucleus and electron–electron interactions are treated classically. Within this model, the kinetic energy of the electrons is defined as,

$$T[\mathbf{n}] = C_F \int n^{5/3}(\mathbf{r}) d\mathbf{r}, \quad \text{with} \quad C_F = \frac{3}{10}(2\pi^2)^{2/3} = 2.871. \quad (3.1.11)$$

From the above equation, an approximation is made that the kinetic energy of the electrons depends exclusively on the electron density. By adding the interaction between electron–nucleus and electron–electron, a total energy in terms of electron density is obtained as

$$E[n] = C_F \int n^{5/3}(\mathbf{r}) d\mathbf{r} - Z \int \frac{n(\mathbf{r})}{r} d\mathbf{r} + \frac{1}{2} \iint \frac{n(\mathbf{r}_1)n(\mathbf{r}_2)}{|\mathbf{r}_1 - \mathbf{r}_2|} d\mathbf{r}_1 d\mathbf{r}_2. \quad (3.1.12)$$

The second and third terms are the electron–nucleus and electron–electron interactions, respectively. The importance of this simple Thomas-Fermi model is not how well it performs in computing the ground state energy and density but more as an illustration that the energy can be determined purely using the electron density.

### Hohenberg-Kohn Theorem

In 1964, Hohenberg and Kohn first derived the fundamentals of density-functional theory which allows to express electronic Hamiltonian as a functional of  $n(\mathbf{r})$ <sup>[73](#)</sup>. This formally relies on two key theorems:

1. There exists a one-to-one correspondence between external potential  $v(\mathbf{r})$  and electron density  $n(\mathbf{r})$ .
2. The ground state electron density can be found by using a variational principle.

In the electronic Hamiltonian only  $V(\mathbf{r})$  depends explicitly on the configuration of the nuclei. If

the first theorem is proven, then from  $n(\mathbf{r})$  one can obtain  $V(\mathbf{r})$  within a trivial additive constant and the whole electronic Hamiltonian can be expressed as a functional of  $n(\mathbf{r})$ . This makes DFT a formal theory and more systematic over Thomas-Fermi model. The proof is done in a simple and extremely elegant manner using the principle of *reductio ad absurdum*, and this is derived for a non-degenerate system. Suppose there is a collection of electrons enclosed into a box influenced by an external potential  $V(\mathbf{r})$ .

Assuming the electron density of this system is known and it also determines  $V(\mathbf{r})$  and thus all properties. If there is another external potential  $V'(\mathbf{r})$  which differs from  $V(\mathbf{r})$  by more than a constant that can also give the same electron density  $n(\mathbf{r})$  for the ground state, then we will have two different Hamiltonians  $\hat{H}$  and  $\hat{H}'$  whose ground state electron density is the same but the normalized wave function  $\Psi$  and  $\Psi'$  would be different. The second Hohenberg-Kohn theorem demonstrates that the ground state energy can be obtained variational, with the density that minimizes the total energy being the exact ground state density. This is expressed as:  $E_0[n_0] \leq E_V[n]$ .

Following from the first part of the theorem, suppose the ground state wave function is  $\Psi$  and its related electron density is  $n(\mathbf{r})$ . Thus the  $n(\mathbf{r})$  uniquely determines the external potential  $V(\mathbf{r})$ . If there is another wave function  $\Psi'$  with an arbitrary variation from  $\Psi$  and its electron density is  $n'(\mathbf{r})$ , then we can obtain,  $\langle \Psi' | \hat{H} | \Psi' \rangle = \int n'(\mathbf{r}) V(\mathbf{r}) d\mathbf{r} + F_{HK}[n'] = E[n'] \geq E[n]$ . So the energy will reach the minimum only when the electron density is the ground-state electron density. If  $F_{HK}[n]$  were a known and sufficiently simple functional of  $n(\mathbf{r})$ , the problem of determining the ground-state energy and density in a given external potential would be rather easy since it requires merely minimization of a functional of the three-dimensional density function. However, it is not and the major part of the complexities of the many-electron problem are associated with the determination of the universal functional  $F_{HK}[n]$ .

### The Kohn-Sham Equations

In 1965, Kohn and Sham published a paper which transformed density-functional theory into a practical electronic structure theory.<sup>74</sup> Kohn and Sham recognized that the failure of Thomas Fermi theory mainly resulted from the bad description of the kinetic energy. To address this problem (similar to the Hartree-Fock approach) they re-introduced the idea of non-interacting electrons moving in an effective field. The functional form of  $F_{HK}[n(\mathbf{r})]$  is written as a sum of the kinetic energy of noninteracting electrons ( $T_s$ ), the Hartree energy ( $E_{\text{Hartree}}$ ), and all the many-body quantum effects are put together into the exchange and correlation energy ( $E_{xc}$ ). So the energy

functional obtained in the previous section now becomes,

$$E[n] = \int n(\mathbf{r})v(\mathbf{r})d\mathbf{r} + F_{HK}[n(\mathbf{r})] = \int n(\mathbf{r})v(\mathbf{r})d\mathbf{r} + Ts[n(\mathbf{r})] + E^{Hartree}[n(\mathbf{r})] + E_{xc}[n(\mathbf{r})]$$

The next step in this electronic structure problem is to define an effective potential,

$$V^{eff} = \frac{\delta \left\{ \int n(\mathbf{r})V(\mathbf{r})d\mathbf{r} + E^{Hartree}[n(\mathbf{r})] + E_{xc}[n(\mathbf{r})] \right\}}{\delta n(\mathbf{r})} = V(\mathbf{r}) + \int \frac{n(\mathbf{r}')}{|\mathbf{r} - \mathbf{r}'|} d\mathbf{r}' + V_{xc}(\mathbf{r})$$

where  $V_{xc}(\mathbf{r})$  is the exchange-correlation potential defined as:  $V_{xc}(\mathbf{r}) = \frac{\delta E_{xc}[n(\mathbf{r})]}{\delta n(\mathbf{r})}$ . This leads to the central equation in Kohn-Sham DFT which is the one-electron Schrödinger like equation expressed as:  $\left[ -\frac{1}{2}\nabla^2 + V^{eff} \right] \phi_i = \epsilon_i \phi_i$ . Here  $\{\phi_i\}$  are the Kohn-Sham one-electron orbitals and the electron density is defined as,  $n(\mathbf{r}) = \sum_{i=1}^N |\phi_i|^2$ .

The  $\epsilon_i$ 's are the energies of the Kohn-Sham one-electron orbitals. Clearly this is a Hartree-Fock-like single particle equation which needs to be solved iteratively. Finally, the total energy can be determined from the resulting density through  $E = \sum_{i=1}^N \epsilon_i - \frac{1}{2} \iint \frac{n(\mathbf{r})n(\mathbf{r}')}{|\mathbf{r} - \mathbf{r}'|} + E_{xc}[n] - \int V_{xc}(r)n(r)d\mathbf{r}$  equations and are the celebrated Kohn-Sham equations. The Kohn-Sham equation must be solved self consistently.

The general procedure is to begin with an initial guess of the electron density, construct the  $V^{eff}$  and then get the Kohn-Sham orbitals. Based on these orbitals, a new density is obtained and the process repeated until convergence is achieved. Finally, the total energy will be calculated with the final electron density. If each term in the Kohn-Sham energy functional was known, we would be able to obtain the exact ground state density and total energy. Unfortunately, there is one unknown term, the exchange correlation (xc) functional ( $E_{xc}$ ).  $E_{xc}$  includes the non-classical aspects of the electron-electron interaction along with the component of the kinetic energy of the real system different from the fictitious non-interacting system. Since  $E_{xc}$  is not known exactly, it is necessary to approximate it, which is the focus of the next section.

### Exchange-Correlation Functionals

**Local-Density Approximation (LDA)** In this approach a real inhomogeneous system is divided into infinitesimal volumes and the electron density in each of the volumes is taken to be constant. The exchange correlation energy for the density within each volume is then assumed to be the exchange correlation energy obtained from the uniform electron gas for that density. The correlation energy is more complicated and generally obtained by fitting to the many-body studies of Gell-Man and Brueckner as well as Ceperly and Alder. Modern LDA functionals tend to be exceedingly similar, differing only in how their correlation contributions have been fitted to the many-body free

electron gas data. The Perdew-Zunger (PZ), Perdew-Wang (PW), and Vosko-Wilk-Nusair (VWN) functionals are all common LDA functionals.

Strictly, the LDA is valid only for slowly varying densities. Indeed LDA works surprisingly well, especially for metals. A partial explanation for this success of the LDA is systematic error cancellation: Typically, in inhomogeneous systems LDA underestimates correlation but overestimates exchange, resulting in unexpectedly good values of  $E_{xc}^{LDA}$ . This error cancellation is not accidental, but systematic, and caused by the fact that for any density the LDA satisfies a number of so-called sum rules. However, recent studies have shown that LDA tends to overestimate cohesive energies by  $\sim 15 - 20\%$  and underestimates lattice constants by  $\sim 2 - 3\%$  for metals and insulators. Problem with LDA becomes more severe for weakly bonded systems, such as vdW and H-bonded systems. For example, the binding energy of the water dimer and the cohesive energy of bulk ice are both  $> 50\%$  too large with LDA compared to the experimental values.<sup>75</sup> Also long range vdW interactions are completely missing in LDA.

**The Generalised Gradient Approximation (GGA)** It was realized very early that only the local uniform density at each given point is not a reasonable approximation for the rapidly varying electron densities of many materials and that the gradient of the density ( $\nabla n(\mathbf{r})$ ) needs to be included. A first attempt was the so-called gradient-expansion approximations (GEA), where one tries to systematically calculate gradient corrections of the form  $|\nabla n(\mathbf{r})|$ ,  $|\nabla n(\mathbf{r})|^2$ ,  $|\nabla^2 n(\mathbf{r})|$ , etc., to the LDA. In practice, the inclusion of low-order gradient corrections almost never improves on the LDA and often even worsens it.

Higher-order corrections are exceedingly difficult to calculate. Eventually it was found that instead of power-series-like gradient expansions one could apply more general functions of  $n(\mathbf{r})$  and  $\nabla n(\mathbf{r})$ . Such functionals of the general form  $E_{xc}^{GGA}[n] = \int f^{GGA}(n(\mathbf{r}), \nabla n(\mathbf{r})) d\mathbf{r}$  are the second generation functional known as GGAs. GGAs are often called "semi-local" functionals due to their dependence on  $\nabla n(\mathbf{r})$ . For many properties, for example, geometries and ground state energies of molecules and solids, GGAs can yield better results than the LDAs. Especially for covalent bonds and weakly bonded systems many GGAs are far superior to LDA. Overall, because of flexibility in the choice of  $f^{GGA}$ , a zoo of GGA functionals have been developed and depending on the system under study, a wide variety of results can be obtained.

The functional form of  $f^{GGA}$  is taken as a correction to the LDA exchange and correlation while (again) ensuring consistency with known sum rules. Within GGA the exchange energy takes the form  $E_x^{GGA}[n] = \int n(\mathbf{r}) \epsilon_x^{unif}(n(\mathbf{r})) F_x^{GGA}(s) d\mathbf{r}$ .  $F_x^{GGA}(s)$  is the exchange enhancement factor and tells how much exchange energy is enhanced over its LDA value for a given  $n(\mathbf{r})$ .

**DFT+U Method** The DFT+U method was first developed in the early 1990s to deal with strongly correlated systems. Depending on whether LDA or GGA is used in practice, the name of LDA+U or GGA+U is referred in literature. As a leading correction to LDA and GGA, the DFT+U method has been proved to be successful in transition metal oxides. The key concept of DFT+U is to address the on-site coulomb interaction in the localized *d* or *f* orbitals with an additional Hubbard type term. At the GGA+U level, the total energy can be summarized in the following form,

$$E_{xc}^{GGA+U}[n, \eta] = E_{xc}^{GGA}[n] + E^{hubbard}[\eta] - E_{dc}[\eta] \equiv E_{xc}^{GGA}[n] + E_u[\eta]$$

where  $n$  refers to the electron density and  $\eta$  is the on-site occupation matrix for *d* or *f* orbitals. The Hartree-Fock like term  $E^{hubbard}[\eta]$  is derived from the Hubbard model and the double counting term  $E_{dc}[\eta]$  addresses on-site interactions for *d* or *f* electrons in LDA. The combination of these two terms is generally referred to the U correction  $E_u[\eta]$  to LDA or GGA.

### Basis Sets

In this section, the concept of the basis set will be introduced. Basis sets are almost always necessary to practically solve the electronic Schrödinger equation. Essentially, almost all electronic structure methods today rely on an expansion on the unknown wave function in terms of a set of basis functions. Any type of basis function may in principle be used like exponential, Gaussian, polynomial, plane-wave, spline, Slater type orbitals, numeric atomic orbitals, etc. However, some issues are useful to consider when selecting basis functions.

The basis functions should allow for the wave function/density to be accurately described with as low a computational cost as possible. The behavior of the basis functions will ideally capture some of the physics of the problem. For example, for bound atomic or molecular systems this means functions should go to zero when the distance between the nucleus and the electron becomes large. In condensed matter systems basis functions with a periodicity matching the crystal lattice can be useful.

For these and other reasons atom centered orbitals like Gaussian functions become very popular in the calculations of chemical problems. The plane wave basis sets were used in the present study which are very popular for electronic structure calculations of condensed matter systems.

### Plane Waves

For the treatment of periodic systems, like solids, plane wave basis sets have become the natural choice because of Bloch's theorem. In a periodic potential,  $U(r)$ , where  $U(r + R) = U(r)$  and  $R$  is the Bravais lattice vector, Bloch's theorem says that the eigen functions of the one-electron Hamiltonian  $H = -\frac{1}{2}\nabla^2 + U(r)$  can be written as a product of a plane wave ( $e^{i\mathbf{k}\cdot r}$ ) and a function,  $\mu_{n,\mathbf{k}}(r)$ , having

the same periodicity as the potential  $U(r)$ :  $\varphi_{n,\mathbf{k}}(r) = e^{i\mathbf{k}\cdot r} \mu_{n,\mathbf{k}}(r)$ , where  $\mu_{n,\mathbf{k}}(\mathbf{r} + \mathbf{R}) = \mu_{n,\mathbf{k}}(\mathbf{r})$ .

Here the index  $\mathbf{k}$  represents a set of plane waves within each primitive unit cell and for each  $\mathbf{k}$  the index  $n$  is a second quantum number, the so called "band index". Bloch's theorem allows to expand the electronic wave function in terms of a discrete set of plane waves. But for a periodic solid which has electrons in the order of Avogadro's number the spacing of the  $\mathbf{k}$  points goes to zero and  $\mathbf{k}$  can be considered as a continuous variable.

So far the infinite number of electrons in the solid are accounted for by an infinite number of  $\mathbf{k}$  points and only a finite number of electronic states are occupied at each  $\mathbf{k}$  point. The occupied states at each  $\mathbf{k}$  point contribute to physical quantities such as the electronic potential, electron density, and total energy of the solid. However, the electronic wave functions at  $\mathbf{k}$  points that are very close together will be almost identical. Hence it is possible to represent them over a region of  $\mathbf{k}$  space only by that at a single  $\mathbf{k}$  point. Efficient methods have been devised to choose special finite sets of  $\mathbf{k}$  points, for obtaining an accurate electronic potential, electron density, and total energy. The magnitude of any error in the total energy or the total energy difference due to inadequacy of the  $\mathbf{k}$  point sampling can always be reduced to zero by using a denser set of  $\mathbf{k}$  points. Therefore, it is crucial to test the convergence of the results with respect to the number of  $\mathbf{k}$  points in general.

Now expanding the periodic function,  $\mathbf{k}(r)$  with plane waves whose wave vectors are reciprocal lattice vectors ( $\mathbf{G}$ ) of the periodic crystal:  $\mu_{n,\mathbf{k}}(r) = \sum_{\mathbf{G}} C_{n,\mathbf{G}} e^{i\mathbf{G}\cdot r}$ , so the electronic wave function can be rewritten as  $\varphi_{n,\mathbf{k}}(r) = \sum_{\mathbf{G}} C_{n,\mathbf{k}+\mathbf{G}} e^{i(\mathbf{k}+\mathbf{G})\cdot r}$ . Employing a finite basis set introduces a new source of inaccuracy, which can be reduced by increasing the number of plane waves or  $E_{cut}$ . Therefore, appropriate convergence tests have to be performed in order to find an  $E_{cut}$  that is sufficiently converged to compute the property of interest with the required accuracy.

### Pseudopotentials

It is well established that most physically interesting properties of solids are largely determined by the valence electrons rather than the core electrons. Meanwhile, the deeply bound core electrons within plane-wave basis sets require a huge amount of basic functions for their description. Thus this leads to a contradiction that the less important core electrons will consume a lot of the computational cost. To alleviate this problem, the pseudo potential approximation replaces the strong ionic potential with a weaker pseudo potential.

In general, the pseudo potential formalism have two main purposes. First, to use a much weaker pseudopotential to get rid of core electrons which due to their deep potential would need to be described by many plane-wave basis functions. Second, to eliminate the rapid oscillations of the valence electron wave functions in the core region. It is essential within the pseudo potential scheme that outside the core region the pseudo potential and wave function becomes the same with the

corresponding all-electron ones.

The most common general form of a pseudopotential is,  $V_{ps} = \sum_{\ell m} |Y_{\ell m}\rangle V_{\ell}(r) \langle Y_{\ell m}|$ . One important class of pseudopotentials are so called norm-conserving pseudopotentials. Norm conserving pseudopotentials require that the all-electron and pseudo wave function agree beyond a chosen radius ( $r_c$ ) and that the integrated density inside  $r_c$  for the all-electron wave function and pseudo wave function are the same ("norm conservation").

One issue with the norm-conserving pseudopotentials is that they cannot generate smoother pseudo wave functions than the all-electron one when coming to the first row elements like Oxygen and the localized transition metals like Nickel due to the "norm conservation" rule. To circumvent this difficulty, Vanderbilt made a radical modification to break the norm conservation rule and relax the condition that the pseudo wave function inside the core region must have the same charge (or integrated density) as the all-electron wave function. By this way,  $r_c$  can be chosen to a larger value and the pseudo wave function can be made much softer than the all-electron wave function.

Clearly, this introduces a deficit in the charge inside the core region and it is compensated with additional localized atom-centered charges. The additional charges are defined as the charge difference between the all-electron and pseudo wave functions and for convenience they are also pseudized. This kind of pseudo potential is called an ultrasoft pseudo potential, which enables much lower plane-wave cut-offs to be used in the calculations. The combination of DFT, plane-wave basis set, and pseudo potentials have become a well-established methodology in electronic structure calculations of condensed matter.

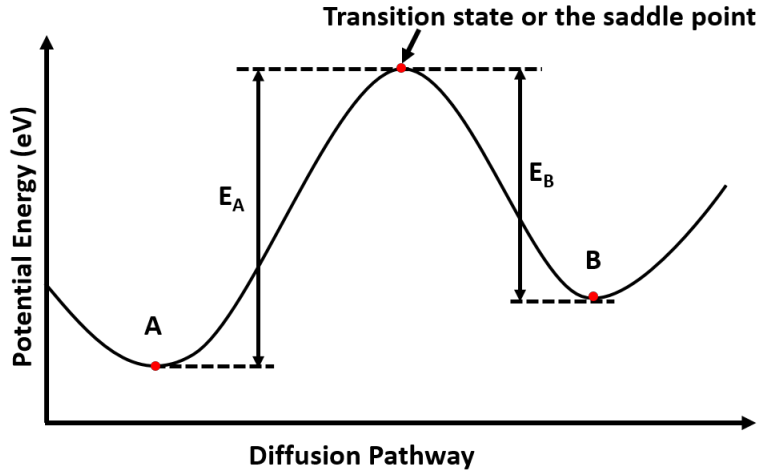
## 3.2. Transition State Search Methods

The transition state of a chemical reaction is a particular structure along the reaction coordinate, which corresponds to a first-order saddle point along the "minimum-energy path" (MEP) on the potential energy surface (PES) and dominates the reaction rate. Transition-state search is quite common and important in condensed matter physics. MEP is the path downwards from the reactant to the product, and it can help us to understand the energetics of the whole reaction process. Various methods for the saddle-point searching have been developed<sup>76</sup>. The Nudged Elastic Band (NEB) Method<sup>77;2</sup> and the Dimer method<sup>78</sup> are discussed here.

### 3.2.1. Nudged Elastic Band Method

The nudged elastic band (NEB) calculation is powerful tool to determine the minimum energy pathway (MEP, Fig. 3.2.1) of two minima on a potential energy surface (PES)<sup>76</sup>. In this work The climbing picture NEB (CI-NEB) approach was used to investigate the diffusion pathways between

two stable adsorption sites, as well as the activation energy barrier relative to the MEP. The following sections presents an introduction to the normal NEB method and the CI-NEB method.

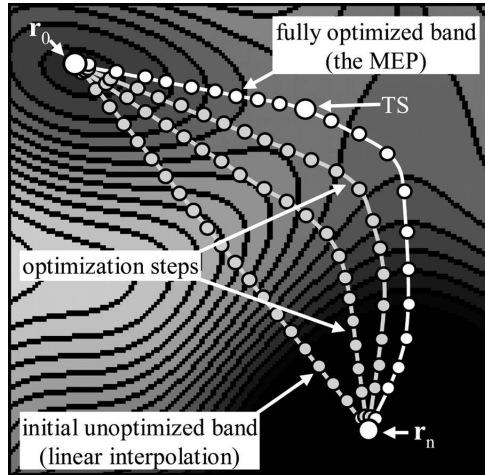


**Figure 3.2.1:** A schematic representation of diffusion in between a stable site A and a stable site B.  $E_A$  and  $E_B$  are the activation barriers from site A and B respectively.

### Normal NEB Method

The NEB method is employed for finding saddle points and MEP between two energy minima: the known reactant and product. The working mechanism for this method comprises linear interpolation of a set of images between the two minima, connection of these images together with springs (forming an elastic band), and then minimizes the energy of each image. Traditional elastic band (EB) method may suffer from two problems: the sliding-down problem and the corner-cutting problem <sup>77</sup>. When a smaller spring constant (for example  $k=0.1$ ) is used to describe the spring force, the true potential force along the path makes the images tend to slide away from the barrier region, giving a low resolution within the saddle point region, which is how the first problem occurs. The second problem is caused by a higher spring constant. For example, when the spring constant equals to 1, the elastic band is too stiff to relax to the saddle point, and the spring force perpendicular to path drives the images to deviate from the true MEP and thus the saddle point region is missed. Obviously, the spring constant has a strong effect on the result, thus the choice of an appropriate spring constant is important. Unfortunately, it is not possible to choose a spring constant to solve the problems mentioned above at the same time. That is why the “nudging” method has been developed, which introduces a force projection scheme to project out the perpendicular component of the spring force and the parallel component of the true potential force. Then, the competitive relation between the spring force and the true potential force is eliminated. Now, the total force on each image

in NEB method is the sum of the true potential force perpendicular to the local tangent and the spring force along the local tangent. Once the energies of these interpolated images minimized, that is, the artificial elastic forces are equal to zero, the mimicked elastic band is the true MEP. The schematic description of NEB method is given in Fig. 3.2.2. The initial and final states are labelled as  $r_0$  and  $r_n$ , respectively. The linearly interpolated image  $r_m$  ( $m=1,2,\dots,N-1$ ) is constructed by

$$r_m = r_0 + m/n(r_n - r_0)$$


**Figure 3.2.2:** A schematic representation of the NEB method. The linear interpolation as the initial pathway, two simulation steps and the final optimized pathway are shown<sup>1</sup>.

Although NEB method could alleviate the two problems caused by the EB method, it still has its own shortcomings. The major drawback is that the transition state is not always located in the images. To obtain the transition state, one way is to simply increase the number of images around the saddle point region, another way is to use the climbing image NEB (CI-NEB) or dimer method as described below.

### Climbing Image Nudged Elastic Band Method

CI-NEB method is a small modification to the NEB method, in which the image with the highest energy is identified as climbing image ( $i_{max}$ ) and located at the saddle point. This image is treated particularly that it does not feel the spring force and the true potential force along the path is inverted. Now, the force acting on  $i_{max}$  is given by<sup>2</sup>,

$$\mathbf{F}_{i_{max}} = -\nabla E(\mathbf{R}_{i_{max}}) + 2\nabla E(\mathbf{R}_{i_{max}})|_{\parallel}$$

where  $E$  is the system's energy,  $R$  represents the position of the intermediate image and  $2\nabla E$  ( $\mathbf{R}_{i_{\max}}\right|_{\parallel}$ ) is the opposite of the true potential force parallel to the elastic band.

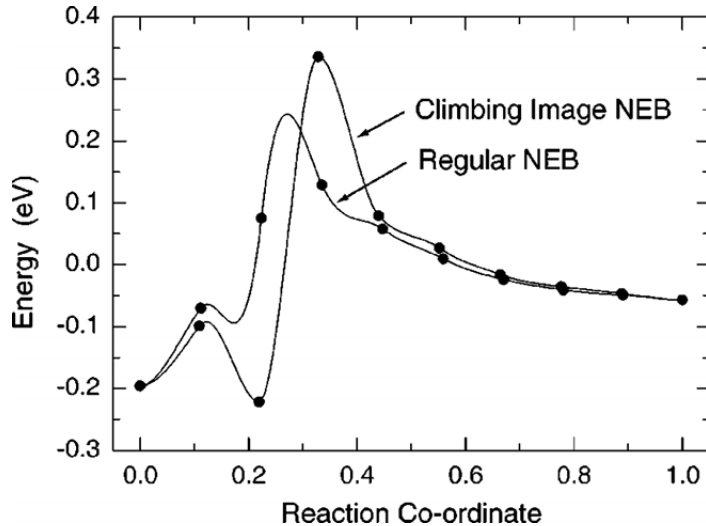


**Figure 3.2.3:** Comparison of the result obtained by regular NEB and CI-NEB method for  $\text{CH}_4$  dissociation on Ir(111) surface.<sup>2</sup>

The reversed force can make the climbing image to an energy minimum in all directions perpendicular to the path and an energy maximum along the path. Therefore, as long as the climbing image converges under this condition, it would be the exact saddle point. It should be noted that the image spacing is no longer equal in CI-NEB method due to the fact that the climbing image is not subjected to the spring force. Henkelman *et al.*<sup>2</sup> gave an example about the  $\text{CH}_4$  molecule dissociated on the Ir(111) surface for comparing the calculated results from NEB and CI-NEB method, as shown in Fig. 3.2.3. Both methods involve eight images, and the computational costs are more or less the same. In particular, the CI- NEB method only needs less than 10% more additional computational costs than the NEB method according to their study. It can be seen clearly from Fig. 3.2.3 that NEB gives a low resolution of the saddle point region and underestimates the activation energy. On the contrary, with the CI-NEB method, it is possible to locate the climbing image at the saddle point and to give a precise barrier. Obviously, CI-NEB method is better than the regular NEB method in searching transition state, which makes it be a more appropriate choice for us to study the chemical reaction and to find the corresponding transition state.

### 3.2.2. The Dimer Method

The dimer method is a transition-state search approach for the unknown reaction mechanism<sup>78</sup>. The advantage for this method is its effectiveness due to the fewer images required for the calculation

and the final structure is not needed to know for performing the calculation. Except for finding the possible saddle points on a MEP, it can also be used to refine a good guess of a transition structure obtained by NEB method. The dimer method works by moving a pair of images (named as “dimer”) uphill from the initial position to search a nearby saddle point on the potential energy surface. Each move contains two movements: rotating and translating the dimer. Each step when the dimer is displaced, the rotational force (the net force on the two images) will make the dimer rotate and to find the direction of lowest curvature. As the dimer rotated to its lowest curvature direction, the net translational force will bring the dimer to a minimum. Since the saddle point is a maximum along the lowest curvature direction, an effective force is introduced to avoid this problem, which can make the dimer translate to the effective force direction and bring the dimer to the saddle point. The effective force here is defined as the opposite of the force component along the dimer, which is similar to that in CI-NEB method.

However, this transition state search method is highly relied on the initial guess for the orientation of the dimer, different initial direction may lead to different saddle point. For example, if a dimer starting from the initial basin which is surrounded by other saddle point basins, the dimer method may not be able to find the expected saddle point but its adjacent saddle point. A general way to use the dimer method in VASP for finding the saddle point usually starts from an NEB calculation, from which the initial configuration and direction along the dimer could be generated as a starting point for the dimer method. This pre-calculation is beneficial for the subsequent search process. Compared with the CI-NEB method, the dimer method requires fewer images, so it would be relatively more efficient. If one wants to do a higher energy cutoff or a finer k-point mesh test based on the obtained transition state by CI-NEB method, the dimer method would be a good choice.

### 3.3. First Principle Calculations of Battery Properties

By solving the Kohn-Sham equations we can obtain important properties of materials for electrochemical applications. The following section briefly describes the basic ideas on how battery properties, specifically equilibrium cell voltage and ionic diffusivity are obtained from first principle calculations.

#### 3.3.1. Intercalation/Deintercalation Voltage

The equilibrium intercalation voltage is determined by the difference in the chemical potential,  $\mu_A$ , of the working ions in the anode and the cathode

$$V = -\frac{\mu_A^{\text{cathode}} - \mu_A^{\text{anode}}}{zF}$$

where  $A$  is the working ion,  $z$  is the charge transferred and  $F$  is the Faraday constant. When the anode is pure metallic Li or Mg,  $\mu_A^{\text{anode}}$  is a constant and the voltage only depends on the chemical potential of the ions in cathode. Integrating, the above equation we can get the average voltage as a function of the free energy of the reaction,

$$\bar{V} = -\frac{\Delta G_r}{zF}$$

where  $\Delta G_r$  is the Gibbs free energy for the overall reaction. At low temperatures the contribution from the entropy is very small and the free energy can be approximated as the internal energy of the reaction,  $\Delta G_r \approx \Delta E_r$ .

Thus, the average voltage of a reaction,  $A_{x1}B \longrightarrow A_{x2}B + (x_1 - x_2)A$  can be computed using,

$$\bar{V}(x_1, x_2) \approx -\frac{E(A_{x1}B) - E(A_{x2}B) - (x_1 - x_2)E(A)}{(x_1 - x_2)F} \quad (3.3.1)$$

where  $A_xB$  is an intercalation cathode with  $A$  as the working ion which may be Li or Mg. Here, the energies of the intercalated and deintercalated phases,  $E(A_{x1}B)$  and  $E(A_{x2}B)$ , and of the metallic Li or Mg can be computed from first principles<sup>79</sup>.

### 3.3.2. Ionic Diffusivity

Diffusion is a non equilibrium phenomenon that refers to the transport of atoms over a chemical potential gradient. During ionic diffusion, ions spend most of their time at the equilibrium sites of the crystal, and only a small fraction of time on the paths connecting the adjacent equilibrium sites. Therefore, the ionic motion can be considered as a succession of discrete hops. To obtain the ionic diffusivity, it is necessary to calculate the frequency with which ions hop between adjacent sites. A good estimation of the hop frequency is given by the transition state theory, in which the hop frequency is given as,

$$k(T) = v^*(T)e^{-\frac{\Delta G^\ddagger(T)}{k_B T}} \quad (3.3.2)$$

where  $v^*$  is a temperature dependent effective attempt frequency,  $k_B$  is the Botzmann constant and  $T$  is the temperature.  $\Delta G^\ddagger$  is the free energy of activation, *i.e.*, the free energy difference of the initial state and the transition state. If we neglect the entropy change,  $\Delta G^\ddagger$  can be approximated as the activation barrier,  $\Delta E_b = E^\ddagger - E_i$ , where  $E^\ddagger$  and  $E_i$  are the energies of the transition state and the initial state respectively. If the hopping distance  $a$  is known, the ionic diffusivity in the dilute limit can be approximately obtained as<sup>79</sup>,

$$D(T) = a^2 k(T) \quad (3.3.3)$$

The Nudged Elastic Band (NEB) method and the Dimer method can be used to find the activation barrier of the diffusion process. These methods have been discussed in the previous sections.

# Chapter 4

## Computational Details

In this work, all the ab-initio calculations were performed by using the Vienna ab initio Simulation Package (VASP),<sup>80</sup> program based on the Density Functional Theory (DFT). This chapter gives an introduction to Vienna ab initio Simulation Package (VASP) and summarizes the details of the first principles calculations of the electronic structure.

### 4.1. Introduction to VASP

VASP is a user friendly complex package for performing *ab-initio* quantum-mechanical molecular dynamics (MD) simulations using pseudopotentials or the projector-augmented wave method and a plane wave basis set. The approach implemented in VASP is based on the (finite-temperature) local-density approximation with the free energy as variational quantity and an exact evaluation of the instantaneous electronic ground state at each MD time step. VASP uses efficient matrix diagonalization schemes and an efficient Pulay/Broyden charge density mixing.

These techniques avoid all problems possibly occurring in the original Car-Parrinello method, which is based on the simultaneous integration of electronic and ionic equations of motion. The interaction between ions and electrons is described by ultra-soft Vanderbilt pseudopotentials (US-PP) or by the projector-augmented wave (PAW) method. US-PP (and the PAW method) allow for a considerable reduction of the number of plane-waves per atom for transition metals and first row elements. Forces and the full stress tensor can be calculated with VASP and used to relax atoms into their instantaneous ground-state.

As VASP uses the PAW method or ultra-soft pseudopotentials, the size of the basis-set can be kept very small even for transition metals and first row elements like C and O. Generally not more than

100 plane waves (PW) per atom are required to describe bulk materials, in most cases even 50 PW per atom will be sufficient for a reliable description. VASP uses a rather "traditional" and "old" fashioned" self-consistency cycle to calculate the electronic ground-state. The combination of this scheme with efficient numerical methods leads to an efficient, robust, and fast scheme for evaluating the self-consistent solution of the Kohn-Sham functional. The implemented iterative matrix diagonalisation schemes (RMM-DIIS and blocked Davidson) are probably among the fastest schemes currently available. VASP includes a full featured symmetry code which determines the symmetry of arbitrary configurations automatically.

The symmetry code is also used to set up the Monkhorst Pack special  $\mathbf{k}$ - points allowing an efficient calculation of bulk materials, symmetric clusters etc. The integration of the band-structure energy over the Brillouin zone is performed with smearing or tetrahedron methods. For the tetrahedron method, Bloch's corrections, which remove the quadratic error of the linear tetrahedron method, can be used resulting in a fast convergence speed with respect to the number of special points. VASP has the most importantly four input files i.e. **INCAR**, **POSCAR**, **POTCAR**, **KPOINTS** and their special features are as follows.

## **INCAR**

The INCAR file is the central input file of VASP. It determines 'what to do and how to do it'. It is a tagged format free-ASCII file: Each line consists of a tag (i.e. a string) the equation sign '=' and one or several values. Defaults are supplied for most parameters. A default for the energy cutoff is for instance given in the POTCAR file, and therefore usually not required in the INCAR file.

## **POSCAR**

The POSCAR file contains the scaling parameter, lattice translational vectors and the positions of the ions. The positions can be given in direct (fractional) or Cartesian coordinates. In the second case, positions will be scaled by the universal scaling factor. The lattice vectors are always scaled by the universal scaling factor.

## **KPOINTS**

The KPOINTS file determines the  $\mathbf{k}$ -point grids to be used to generate the  $\mathbf{k}$ -points for the SCF calculations. There are several settings available in the KPOINTS file to generate the  $\mathbf{k}$ -points depending upon our need that include special  $\mathbf{k}$ -point method, tetra hedron method etc. The  $\mathbf{k}$ -points are generated automatically using the Monkhorst-Pack's technique with the supplied KPOINTS file (like 4x4x4) Monkhorst-Pack grid is used for most of the calculation.

## POTCAR

The POTCAR file contains the pseudo potentials. The POTCAR file also contains information about the atoms (i.e. their mass, their valence, the energy of the atomic reference configuration for which the pseudo potential was created etc.)

## 4.2. Methodology

All the ab-initio calculations were performed by using the Vienna ab initio Simulation Package (VASP) program based on the Density Functional Theory (DFT). The Perdew Burke Ernzerhof (PBE) exchange and correlation functionals was used within the GGA+U level with Projector Augmented Wave (PAW) method. VdW-DF2 functional<sup>81, 82</sup> and D2 method of Grimme<sup>83, 82</sup> was used to properly account the van der Waals-based interlayer interaction<sup>84</sup>. The U (on-site coulomb term) for Vanadium was selected as 4 eV, which was used from the Materials Project. Tin doping with oxygen vacancy was introduced in a 1 x 3 x 3 supercell and calculations were carried out using Gamma-point sampling. The plane wave basis set energy cutoff was set at 520 eV. Spin polarization is included in the calculations.

NEB calculations were done as implemented in VASP using the VTST tools provided by Henkelman *et al.* The Climbing image NEB method was done using DFT without the Hubbard U term. For  $\alpha\text{-V}_2\text{O}_5$  4 images were used to converge the images. The images were considered converged, when the force on every ion is less than  $0.05 \text{ eV}\text{\AA}^{-1}$ .

# Chapter 5

## First Principle Study of Sn doped $V_2O_5$ with Oxygen Vacancy as Cathode Material for Magnesium Batteries

### 5.1. Literature review

#### 5.1.1. Introduction

The vanadium pentoxide  $V_2O_5$  got huge attention due to its outstanding performance in lithium battery applications. It offers exciting properties of being a reversible intercalating cathode for Mg batteries. Because of its spin ladder properties and well-known Li intercalation properties, the orthorhombic  $V_2O_5$  structure has been well-characterized, with a reversible capacity of 130 mAh/g and a voltage of 3.3 V vs Li metal. Many studies have also investigated intercalation of Mg into  $V_2O_5$ .<sup>85</sup> The most significant advantage of switching  $V_2O_5$  to multivalent systems is the increase in volumetric energy density (3833 mAh/cm<sup>3</sup> for Mg). This is one of the most studied cathode materials that shows promising Mg intercalation other than  $Mo_3S_8$  and  $MoO_3$  discussed earlier in chapter 2.

The structure of  $V_2O_5$  can be viewed as a series of layers perpendicular to (001) direction with weak van waals interaction between layers. Each layer is composed of square  $VO_5$  pyramids which share

edges and corners. pyramids share an edge and have an opposite orientation in the c direction. There are three types of inequivalent oxygen atoms: apical oxygens (O1) and bridging oxygen atoms (O2), as well as chaining oxygen atoms (O3), which act as bridges between three  $\text{VO}_5$  square pyramids (see fig.5.1.1)

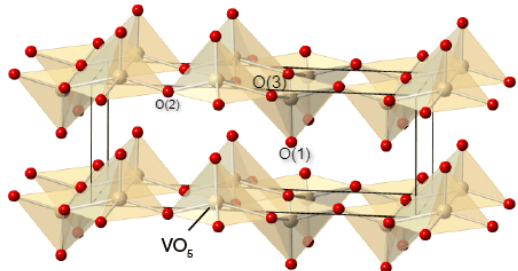


**Figure 5.1.1:** Crystal structure of  $\text{V}_2\text{O}_5$ . Vanadium atoms are in brown color, while oxygen atoms are in red color<sup>3</sup>

### 5.1.2. Polymorphs of $\text{V}_2\text{O}_5$

Li intercalation into  $\text{V}_2\text{O}_5$  has been investigated extensively both experimentally<sup>86</sup> and theoretically.<sup>87</sup> However there are significantly less studies of Mg intercalation. So far experimental reports have succeeded in reversibly inserting only about half a Mg ( $x_{\text{Mg}} = 0.5$ ) per formula unit of  $\text{V}_2\text{O}_5$ , where as up to  $x_{\text{Li}} = 3$  has been inserted per  $\text{V}_2\text{O}_5$ . Gregory et al.<sup>88</sup> have showed Mg insertion up to  $\text{Mg}_{0.66}\text{V}_2\text{O}_5$ .<sup>89</sup> Here we represent the different polymorphs(see fig.5.1.2 based on the intercalation of Li in  $\text{V}_2\text{O}_5$ ). Their differences lie in the arrangements of atoms in the unit cells. The structure of bulk  $\text{V}_2\text{O}_5$  is called  $\alpha$ - $\text{V}_2\text{O}_5$ . At low concentrations of Li in  $\text{V}_2\text{O}_5$ , the structure changes to the  $\epsilon$  phase. The structure of  $\text{Li}_x\text{V}_2\text{O}_5$  for  $x \leq 0.13$  is the  $\alpha$  phase and for  $0.3 \leq x \leq 0.8$  it is the  $\epsilon$  phase, both of which are of the same space group  $Pmmn$ . At high concentrations of Li, *i.e.*, for  $\text{Li}_x\text{V}_2\text{O}_5$  for  $0.88 \leq x \leq 1.0$ , the structure transforms to the  $\delta$  phase with  $Cmcm$  space group. Finally, with even further lithiation, in the Li range  $1.0 < x < 2.0$  of  $\text{Li}_x\text{V}_2\text{O}_5$ , the  $\gamma$ -phase is stabilized with a space group symmetry of  $Pnma$ .<sup>4</sup>

The main difference between the  $\delta$  phase and the  $\alpha$  phase is a translation of alternating  $\text{V}_2\text{O}_5$  layers in the a-direction by “a/ 2”, which doubles the “b” lattice parameter (as well as the unit cell) of the  $\delta$  phase. The Mg sites in both  $\alpha$  and  $\delta$  are situated near the middle of the VO<sub>5</sub> pyramids (along a) and between the 2 layers (along b). As a result of shifting of layers between the  $\alpha$  and  $\delta$  phases, the anion coordination environment of the Mg sites also changes. Considering a Mg-O bond length cutoff of 2.5 Å, the Mg in the  $\alpha$  phase is 8-fold coordinated (4 nearest neighbor O atoms and 4

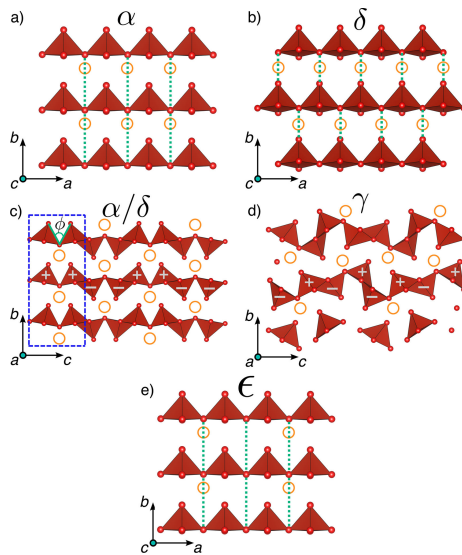


**Figure 5.1.2:** (a)  $\alpha$  and (b)  $\delta$  polymorphs of orthorhombic  $V_2O_5$  are shown along the  $c$ -axis. (c) along the  $a$ -axis which is compared to the (d)  $\gamma$  polymorph, has a different orientation of  $VO_5$  pyramids and the dashed blue rectangle in panel (c) indicates a distance of  $c/2$ . Panel (e) illustrates the  $\epsilon$  phase.<sup>4</sup>

next-nearest neighbors,  $4 + 4$ ) whereas the Mg in the  $\delta$  phase is 6-fold coordinated ( $4 + 2$ ).<sup>90</sup> The  $\epsilon$  phase is a specific ordering of Mg atoms on the  $\alpha$ - $V_2O_5$  host at half magnesiation. The  $VO_5$  pyramids in the  $\alpha$  and  $\delta$  phases “pucker” upon Li intercalation, as observed experimentally by Cava et al.<sup>91</sup>. Theoretical calculations<sup>4</sup>, supported by experimental data suggest stability of  $\alpha$  phase of  $V_2O_5$  structure upon Mg intercalation.<sup>92</sup> Our calculations focus particularly on Mg intercalation in  $\alpha$ - $V_2O_5$ .

### 5.1.3. Effect of Sn-doping in $V_2O_5$ Cathode Materials

While the  $V_2O_5$  cathode material has a promising Li-ion capacity, it has a number of drawbacks, including poor structural stability, low electronic and ionic conductivity, and sluggish electrochemical kinetics. Various approaches have been found to improve these drawbacks. Doping foreign atoms such as Cr, Fe, Cu, Al and Sn into the  $V_2O_5$  lattice structure have been found to boost the electrochemical performance. Sn-doped  $V_2O_5$  shows substantial enhancement of Li-ion storage in terms of kinetics and stability. Small amount of Sn (5%) into the  $V_2O_5$  film increases the electrochemical reaction reversibility and Li-ion diffusivity. The reason may be the formation of reduced V ions ( $V^{4+}$ ) which help in enhancing conductivity by improving the intercalation.<sup>93</sup> Sn doping in  $V_2O_5$  lattice could be done in two different ways; that is Sn could insert between the  $V_2O_5$  layers or substitute at lattice V sites. Li et al.<sup>94</sup> proposed the substitutional Sn doping by replacing the V ions at the lattice sites. It also induces the formation of oxygen vacancies. Recent

studies have shown that oxygen vacancy in electrode materials will enhance their properties in a favorable way for batteries. Oxygen vacancies can help to maintain the structure during insertion and extraction ions such that the cycling performance is enhanced compared to pristine electrode materials.<sup>95</sup>

## 5.2. Results and Discussions

### 5.2.1. Structural Details

In order to study the impact of Sn doing toward the electrochemical performance of  $V_2O_5$  cathode material, we first optimized the lattice parameters of  $\alpha V_2O_5$  and  $\alpha MgV_2O_5$ . Bulk vanadium pentoxide  $V_2O_5$  forms a simple orthorhombic layer crystal with space group Pmmn with lattice constants  $a = 11.544 \text{ \AA}$ ,  $b = 3.571 \text{ \AA}$ . and  $c = 4.383 \text{ \AA}$ . The physical layers are composed of distorted  $VO_5$  pyramids sharing edges and corners, as shown in Fig. 5.1.1. We used the VdW-DF method<sup>81, 82</sup> and D2 method of Grimme<sup>83, 82</sup> in combination with the PBE+U functional to properly account weak van der Waals attraction between  $V_2O_5$  layers.

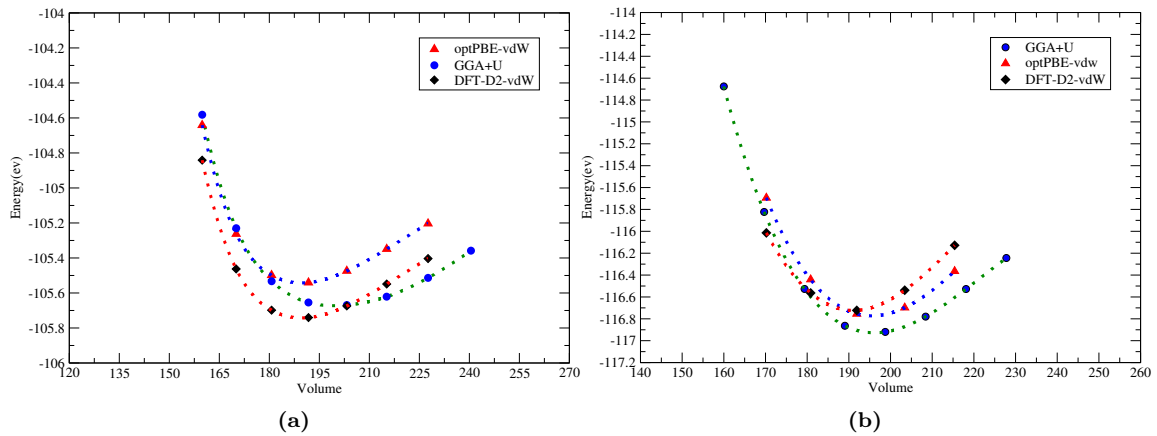


**Figure 5.2.1:** The total Energy vs Volume curve for (a)  $V_2O_5$  (b)  $\alpha MgV_2O_5$

Our calculated lattice parameters and V-O bond distances, are consistent with those of the experimental values. From the theoretical optimization and the experiments listed in Table 5.2.1, it was found that applying the vdW-DF method to the bulk  $V_2O_5$  gave more accurate predictions of the lattice parameters.

Overestimation of  $c$  parameter (10.4%) is due to the fact that DFT does a poor job of properly accounting the existing van der Waals-based interlayer interaction. We further used the VdW-DF method in other calculations. From table. 5.2.2 it was found that intercalation of Mg ions removes

| parameters        | GGA+U          | DFT-D2-vdW   | OptPBE-VdW   | Exp. <sup>96</sup> |
|-------------------|----------------|--------------|--------------|--------------------|
| a                 | 11.546(0.185%) | 11.619(0.6%) | 11.683(1.2%) | 11.5440            |
| b                 | 3.635(1.7%)    | 3.607(1.0%)  | 3.633(1.7%)  | 3.5710             |
| c                 | 4.841(10.4%)   | 4.474(2.07%) | 4.467(1.91%) | 4.3830             |
| Volume            | 203.2          | 187.58       | 189.63       | 180                |
| $d \vee -o_1$ (Å) | 1.61           | 1.61         | 1.619        | 1.58               |
| $d \vee -o_2$ (Å) | 1.80           | 1.80         | 1.81         | 1.78               |
| $d \vee -o_3$ (Å) | 1.90/2.04      | 1.90/2.04    | 1.91/2.04    | 1.88/2.02          |

**Table 5.2.1:** Comparison of orthorhombic lattice constants a, b, c of bulk V<sub>2</sub>O<sub>5</sub> obtained from experimental measurement versus those from the current calculations. The percentage values give the relative deviation from the experimental value. All values are given in Å.

| parameters | GGA+U          | DFT-D2-vdW    | optPBE-vdW    | Exp. <sup>97</sup> |
|------------|----------------|---------------|---------------|--------------------|
| a          | 11.635 (1.17%) | 11.634(0.77%) | 11.643(0.08%) | 11.5440            |
| b          | 3.431(-4%)     | 3.40(4.8%)    | 3.429(-4%)    | 3.5740             |
| c          | 4.64(5.9%)     | 4.51(2.9%)    | 4.57(4.3%)    | 4.3830             |
| Volume     | 195.6          | 191.08        | 194.60        | 180                |

**Table 5.2.2:** Comparison of orthorhombic lattice constants a, b, c of bulk  $\alpha$ -MgV<sub>2</sub>O<sub>5</sub> obtained from experimental measurement versus those from the current calculations. The percentage values give the relative deviation from the experimental value. All values are given in Å

the Van der Waals force where all three methods predict the lattice parameters close to the experimental values.

### 5.2.2. Electronic Structure

To investigate the electronic structure of the pristine  $\alpha$ V<sub>2</sub>O<sub>5</sub> and  $\alpha$ MgV<sub>2</sub>O<sub>5</sub>, we calculated their partial density of states (PDOS). Figure 5.2.2 shows that calculated PDOS of the pristine  $\alpha$ -V<sub>2</sub>O<sub>5</sub>, exhibits semiconducting behavior with a calculated band gap of 2.20 eV, which is in good agreement with the experimental band gap, 2.30 eV.<sup>98</sup>

From the PDOS of  $\alpha$ -V<sub>2</sub>O<sub>5</sub> (fig.5.2.2a) There were three different bands found. The valence band, which starts at -4.74 eV below the Fermi level, which consists primarily of O 2p states and non-negligible V 3d states. Across the band gap, The conduction band was separated into 2 parts with a small gap of 0.32 eV. Conduction bands are mainly contributed by V 3d states and small admixture of O-2p states. The splitting of the conduction band is theoretically explained as strong deviations of the VO<sub>5</sub> square pyramids from their cubic symmetry.<sup>99</sup> In  $\alpha$ -MgV<sub>2</sub>O<sub>5</sub> (see fig.5.2.2b) a sharp peak has been observed at -0.39 eV in valence band which may be due to the polarisation of nearest V site by inserted Mg ion, the band mainly comprises of V 3d states.

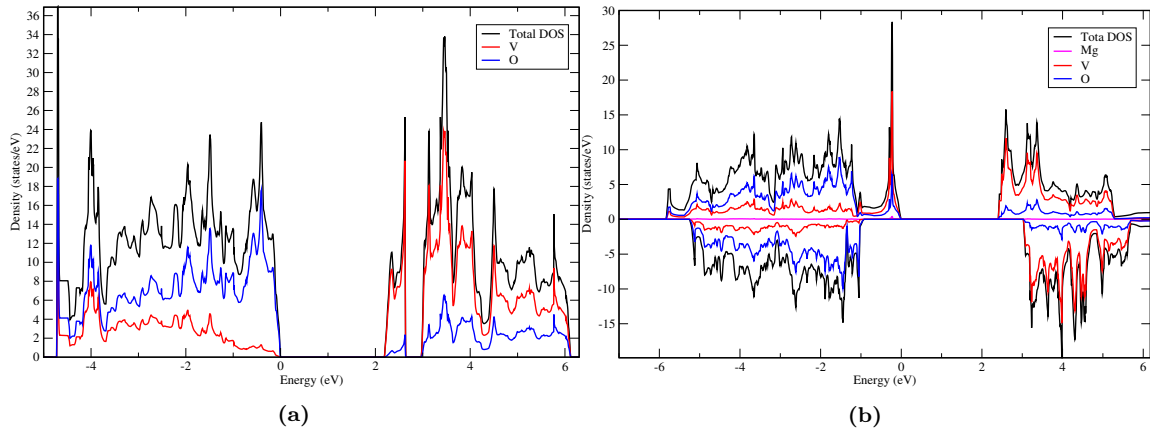


**Figure 5.2.2:** Projected density of states (PDOS) of (a)  $\alpha$ -V<sub>2</sub>O<sub>5</sub> where blue and red lines illustrate states contributed by O 2p and V 3d, respectively (b)  $\alpha$ -MgV<sub>2</sub>O<sub>5</sub>

### Effects of Sn doping in V<sub>2</sub>O<sub>5</sub>

In order to observe the Sn doping effect we first replaced V with Sn from the 1 x 3 x 3 supercell of perfect  $\alpha$ -V<sub>2</sub>O<sub>5</sub>. Due to the occupancy of V<sup>5+</sup> sites with Sn<sup>4+</sup> one oxygen vacancy was created at O(1) site. Oxygen vacancies present in Sn-doped V<sub>2</sub>O<sub>5</sub> can facilitate Mg ion intercalation. In the second case we removed one oxygen at O(2) site thereby replacing two adjacent V atoms by Sn in order to compensate the O<sup>2-</sup> oxidation state. The electronic Density of States (DOS) were calculated for both the cases.

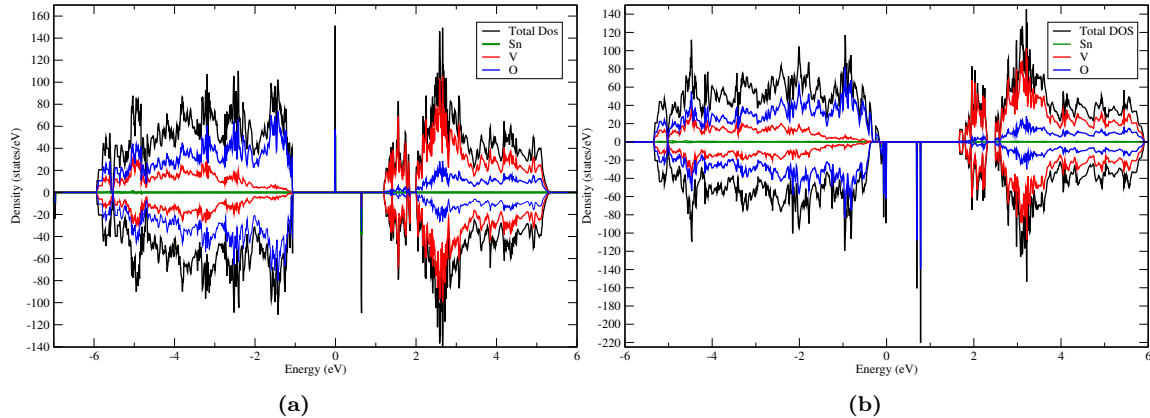


**Figure 5.2.3:** PDOS of Sn doped V<sub>2</sub>O<sub>5</sub> supercell where red, black, and green lines represent states contributed by V, O , and Sn respectively (a) oxygen vacancy at O(1) site with one V atoms replaced (b) oxygen vacancy at O(2) site with two adjacent V atoms replaced

As can be seen from Figure 5.2.3 the intermediate bands can be observed in both the cases. The

band gap of the doped systems decreases from 2.29 eV for pristine  $\text{V}_2\text{O}_5$  to 0.60 eV and 0.68 eV respectively. These intermediate bands mostly consists of O 2p and Sn states, which shows a bonding character between Sn and O atoms. Broadening of conduction bands in both cases is also observed, which further help in decreasing the Band gap. Thus it is found that doping with Sn will boost the electrical conductivity of the  $\alpha\text{-V}_2\text{O}_5$ , which is a good sign for a cathode material.

### 5.3. Activation Barrier for Mg Diffusion and Effect of Sn doping

The migration rate of metal atom has a major impact on the rate performance of electrode materials. The Climbing Image Nudged Elastic Band (CI-NEB) method, discussed earlier in chapter 3, was used to obtain the activation barriers for Mg migration from a stable site to other. Here, the U term was not included as the convergence of DFT+U for NEB calculations is complicated. Furthermore, there is no evidence that DFT+U improves the results compared to normal DFT calculations. The three potential paths for migration of a Mg atom to a nearby vacant site is shown in Fig. 5.3.1.

According to previous literature, Migration of Mg atoms along Path B and C is substantially more difficult than migration via Path A, and migration through these pathways is practically not possible. The reason for this is that migration through Path B requires hopping through the V layers. The V-V distance is only 4.368 Å and electrostatic repulsion from vanadium will significantly increase the energy of mobility along this path. Path C, on the other hand, requires diffusing between the two adjacent channels that are formed of the O1 atom. Thus a Mg ion inserted in  $\text{V}_2\text{O}_5$  is unlikely to diffuse between these channels. Thus, only diffusion through Path A is considered to be favourable and we too considered same path in this work.

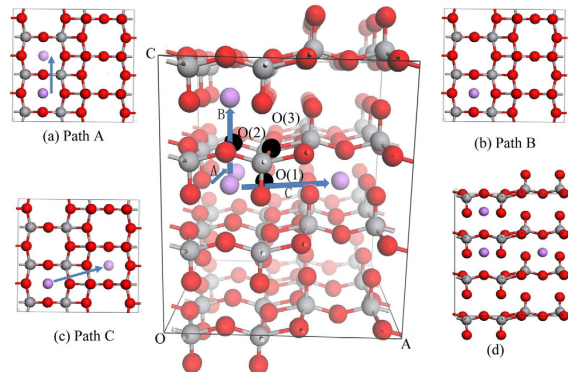


**Figure 5.3.1:** Three potential paths for Mg-ion hopping in  $\alpha\text{-V}_2\text{O}_5$ .

The migration barrier of pristine  $\alpha\text{-V}_2\text{O}_5$  and the reduced systems were computed using the CI-NEB

taking four images between the initial and final state. The activation barriers for the perfect system was found to be  $\sim 0.929$  eV and is in accordance with previous studies, which reported barriers of  $\sim 975\text{-}1100$  meV. For the Sn doped systems with O(1) and O(2) vacancy, we considered the diffusion along the pathway adjacent to the oxygen vacancy i.e. path on the disordered layer(P1). The migration barrier obtained was  $\sim 1.66$  eV and  $\sim 1.76$  eV which is higher than the pristine system. The calculated activation barriers are given in Fig. 5.3.2

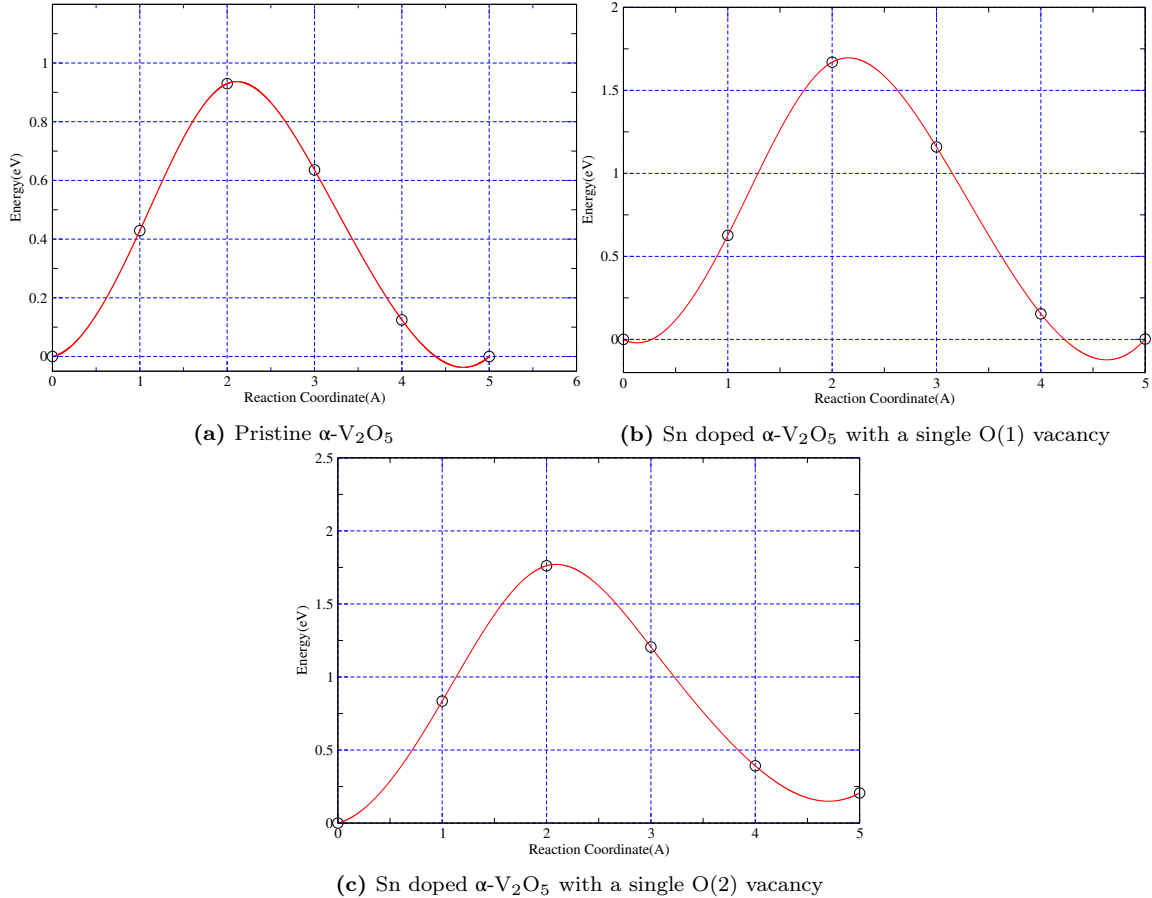


**Figure 5.3.2:** Migration Barriers for  $\alpha$ - $\text{V}_2\text{O}_5$  Path on the disordered layer (P1)

The migration behaviour of Mg in Sn doped  $\alpha$ - $\text{MgV}_2\text{O}_5$  with oxygen vacancy, when computed along the pathway adjacent to the Oxygen vacancy gives a higher activation barrier. This maybe due to the repulsion caused by Sn ion that are larger in size than V ions. The other reason may be the reduction of interlayer spacing corresponding to this pathway due to the oxygen vacancy. When the oxygen vacancy is introduced the repulsion between the top layer decreases. This in turn causes this

layer spacing to decrease. At the same time, the interlayer spacing of the layer below the oxygen vacancy increases. This motivates us to study of the migration behaviour in this layer i.e. path above the disordered layer(P2). Thus, the migration barrier for Mg diffusion through this layer was calculated similar to the above calculations. This gives an activation barrier of 0.56 eV and 0.57 eV for O(1) and O(2) vacancy respectively, which is lower than that of the one obtained for pure  $\alpha$ -MgV<sub>2</sub>O<sub>5</sub>. The calculated activation barriers are given in Fig.5.3.3

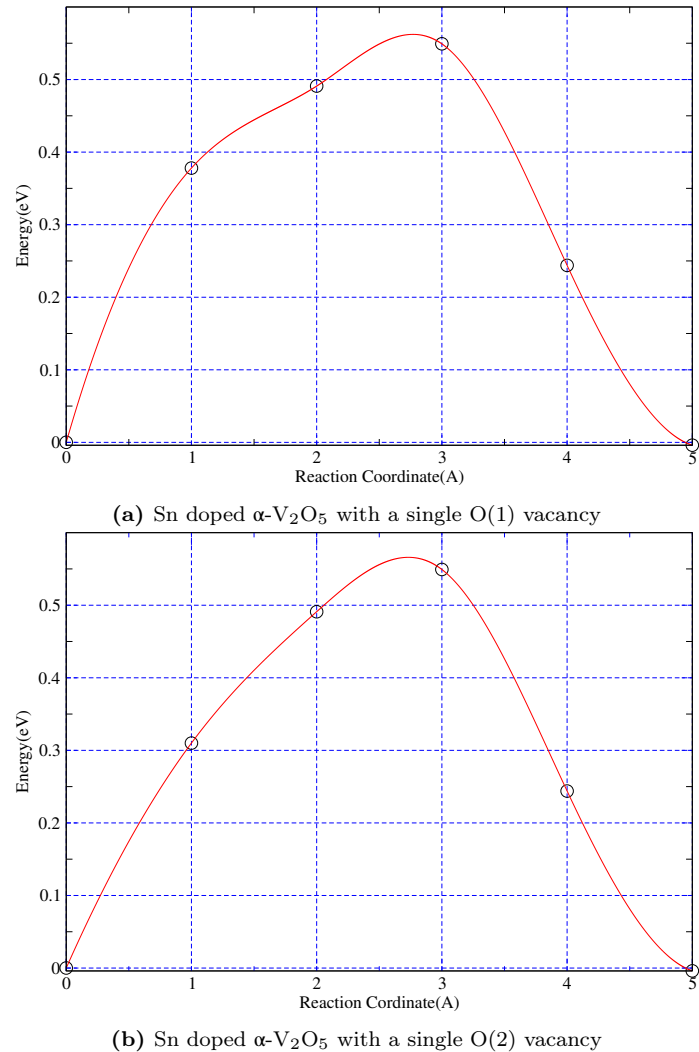


**Figure 5.3.3:** Migration Barriers for  $\alpha$ -V<sub>2</sub>O<sub>5</sub> Path above the disordered layer (P<sub>2</sub>)

## 5.4. Mg-ion Diffusivity

As a cathode material, a critical parameter is the rate of diffusion of intercalated magnesium ions and this determines the power output and battery charging times. As noted earlier in Chapter 3, the diffusivity can be calculated from the activation energy.

$$D(T) = a^2 k(T) = a^2 \nu^*(T) e^{-\frac{\Delta E_b}{k_B T}} \quad (5.4.1)$$

where  $a$  is the hopping distance and  $\nu^*$  is the attempt frequency. The hopping distance in  $\delta\text{-MgV}_2\text{O}_5$  is approximately 3.5 Å. The frequency  $\nu^*$  is about  $3 \times 10^{13}$  Hz as taken from the theoretical work of J.Spitaler et al<sup>100</sup>.

It can be seen that the diifusivity is in the order of  $10^{-11}$ , while the Li diffusivity is about  $4.85 \times 10^{-8} \text{ cm}^2 \text{s}^{-1}$  with the same parameters, except the energy barrier<sup>101</sup>.

|            | Diffusivity ( $\text{cm}^2 \text{s}^{-1}$ ) |   |
|------------|---|---|
|            | $\alpha\text{-V}_2\text{O}_5(\text{P}_1)$   | $\alpha\text{-V}_2\text{O}_5(\text{P}_2)$ |
| Pristine   | $9.19 \times 10^{-18}$                      |   |
| O1 vacancy | $4.86 \times 10^{-30}$                      | $1.44 \times 10^{-11}$                    |
| O2 vacancy | $1.01 \times 10^{-31}$                      | $9.83 \times 10^{-12}$                    |

**Table 5.4.1:** Calculated diffusivity of  $\text{Mg}^{2+}$

## Chapter 6

# Conclusions and Future Outlook

First principle calculations of  $V_2O_5$  with oxygen vacancy was carried out using VdW-DF method and D2 method of Grimmein combination with the PBE+U. Applying the vdW-DF method was found to give the more accurate prediction of the lattice parameters. Intercalation of Mg ions in  $V_2O_5$  was found to eliminate the effect of van der waals interactions. Depending on Mg concentration,  $V_2O_5$  exists in several phases, the  $\alpha$  phase for dilute concentration,  $\epsilon$  phase at intermediate concentrations, and the  $\delta$  phase at high concentrations. In this work, calculations have been done with  $\alpha$ - $V_2O_5$  at the dilute limit. Oxygen vacancy was created at two sites by replacing adjacent Vanadium atom by Tin. From the electronic structure, it is noted that Sn doping along with the oxygen vacancy forms intermediate bands near the valence and conduction band. This causes the reduction in the Band gap which increases the electrical conductivity. Broadening of bands also accompany with the band gap reduction. NEB calculations are done to study Mg mobility behaviour in this material. The migration barrier of both pristine system and the doped system was computed for  $\alpha$ - $V_2O_5$ . For doped system intercalation in same layer of vacancy shows the higher migration barrier for all the systems which shows the sluggish kinetics observed for this cathode in practical applications. Accurate prediction of interlayer distance and repulsion due to Sn ion could be the reason for the higher potential barrier in same layer of oxygen vacancy. It is reduced for the lower layer, due to interlayer spacing expansion/contraction. This motivates us to study the migration behaviour in other  $\delta$  polymorphs of  $V_2O_5$ . Theoretical studies shows the lower barrier potential for  $\delta$  polymorphs. Introduction of dopants and oxygen vacancies could be further utilised to get more reduced barriers. Further research might help to eliminate the problem of slow diffusion in  $V_2O_5$  and other cathode materials, which may lead to a practical rechargeable magnesium battery with low cost and high energy density.

# Bibliography

- [1] Hannes Jónsson, Greg Mills, and Karsten W Jacobsen. Nudged elastic band method for finding minimum energy paths of transitions. 1998.
- [2] Graeme Henkelman and Hannes Jónsson. Improved tangent estimate in the nudged elastic band method for finding minimum energy paths and saddle points. *The Journal of chemical physics*, 113(22):9978–9985, 2000.
- [3] <https://www.chemtube3d.com/ss-v2o5/>.
- [4] Gopalakrishnan Sai Gautam, Pieremanuele Canepa, Aziz Abdellahi, Alexander Urban, Rahul Malik, and Gerbrand Ceder. The intercalation phase diagram of mg in v<sub>2</sub>o<sub>5</sub> from first-principles. *Chemistry of Materials*, 27(10):3733–3742, 2015.
- [5] Qi Guo, Wen Zeng, Shi-Lin Liu, Yan-Qiong Li, Jun-Yao Xu, Jin-Xing Wang, and Yu Wang. Recent developments on anode materials for magnesium-ion batteries: a review. *Rare Metals*, pages 1–19, 2020.
- [6] Fanfan Liu, Tiantian Wang, Xiaobin Liu, and Li-Zhen Fan. Challenges and recent progress on key materials for rechargeable magnesium batteries. *Advanced Energy Materials*, 11(2):2000787, 2021.
- [7] Zihe Zhang, Xu Zhang, Xudong Zhao, Sai Yao, An Chen, and Zhen Zhou. Computational screening of layered materials for multivalent ion batteries. *ACS omega*, 4(4):7822–7828, 2019.
- [8] Matthew M Huie, David C Bock, Esther S Takeuchi, Amy C Marschilok, and Kenneth J Takeuchi. Cathode materials for magnesium and magnesium-ion based batteries. *Coordination Chemistry Reviews*, 287:15–27, 2015.
- [9] Muhammad Rashad, Muhammad Asif, Yuxin Wang, Zhen He, and Iftikhar Ahmed. Recent advances in electrolytes and cathode materials for magnesium and hybrid-ion batteries. *Energy Storage Materials*, 25:342–375, 2020.

- [10] Tianran Zhang, Daixin Li, Zhanliang Tao, and Jun Chen. Understanding electrode materials of rechargeable lithium batteries via dft calculations. *Progress in Natural Science: Materials International*, 23(3):256–272, 2013.
- [11] A Banu, A Sakunthala, M Thamilselvan, P Senthil Kumar, K Suresh, and S Ashwini. Preparation, characterization and comparative electrochemical studies of mgmxmn<sub>2-x</sub>o<sub>4</sub> (x= 0, 0.5; m= ni/co). *Ceramics International*, 45(10):13072–13085, 2019.
- [12] Anu Maria Augustine, Vishnu Sudarsanan, Geo Sunny, and P Ravindran. A first principle study on iron substituted lini (bo<sub>3</sub>) to use as cathode material for li-ion batteries. In *AIP Conference Proceedings*, volume 1942, page 090043. AIP Publishing LLC, 2018.
- [13] David Linden and Thomas B Reddy. Handbook of batteries 3 ed. amerika serikat: The mcgraw-hills com-panies, 2002.
- [14] Hans J Herfurth. Building better batteries. *Industrial Laser Solutions*, 2009.
- [15] John B Goodenough. Changing outlook for rechargeable batteries, 2017.
- [16] Gang Wang, Minghao Yu, and Xinliang Feng. Carbon materials for ion-intercalation involved rechargeable bat-tery technologies. *Chemical Society Reviews*, 2021.
- [17] Naoki Nitta, Feixiang Wu, Jung Tae Lee, and Gleb Yushin. Li-ion battery materials: present and future. *Materials today*, 18(5):252–264, 2015.
- [18] Zhangxian Chen, Weixin Zhang, and Zeheng Yang. A review on cathode materials for advanced lithium ion batteries: microstructure designs and performance regulations. *Nanotechnology*, 31(1):012001, 2019.
- [19] T Nagaura. Lithium ion rechargeable battery. *Progress in Batteries & Solar Cells*, 9:209, 1990.
- [20] Mogalahalli V Reddy, Alain Mauger, Christian M Julien, Andrea Paoletta, and Karim Zaghib. Brief history of early lithium-battery development. *Materials*, 13(8):1884, 2020.
- [21] Mahesh Datt Bhatt and Colm O'Dwyer. Recent progress in theoretical and computational investigations of li-ion battery materials and electrolytes. *Physical Chemistry Chemical Physics*, 17(7):4799–4844, 2015.
- [22] Tsutomu Ohzuku and Atsushi Ueda. Why transition metal (di) oxides are the most attractive materials for batteries. *Solid State Ionics*, 69(3-4):201–211, 1994.
- [23] Masataka Wakihara. Recent developments in lithium ion batteries. *Materials Science and Engineering: R: Reports*, 33(4):109–134, 2001.

- [24] Mehul Oswal, Jason Paul, and Runhua Zhao. A comparative study of lithium-ion batteries. *USA: University of Southen California*, 2010.
- [25] Celine Cluzel, Craig Douglas, et al. Cost and performance of ev batteries. *Final report for the committee on climate change*, 21(03), 2012.
- [26] Michael Heß and Petr Novák. Shrinking annuli mechanism and stage-dependent rate capability of thin-layer graphite electrodes for lithium-ion batteries. *Electrochimica Acta*, 106:149–158, 2013.
- [27] Jasper Biemolt, Peter Jungbacker, Tess van Teijlingen, Ning Yan, and Gadi Rothenberg. Beyond lithium-based batteries. *Materials*, 13(2):425, 2020.
- [28] Erik J Berg, Claire Villevieille, Daniel Streich, Sigit Trabesinger, and Petr Novák. Rechargeable batteries: grasping for the limits of chemistry. *Journal of The Electrochemical Society*, 162(14):A2468, 2015.
- [29] Feixiang Wu, Hyea Kim, Alexandre Magasinski, Jung Tae Lee, Huan-Ting Lin, and Gleb Yushin. Harnessing steric separation of freshly nucleated li<sub>2</sub>s nanoparticles for bottom-up assembly of high-performance cathodes for lithium-sulfur and lithium-ion batteries. *Advanced Energy Materials*, 4(11):1400196, 2014.
- [30] Wei Luo, Fei Shen, Clement Bommier, Hongli Zhu, Xiulei Ji, and Liangbing Hu. Na-ion battery anodes: materials and electrochemistry. *Accounts of chemical research*, 49(2):231–240, 2016.
- [31] Ji Qian, Feng Wu, Yusheng Ye, Menglu Zhang, Yongxin Huang, Yi Xing, Wei Qu, Li Li, and Renjie Chen. Boosting fast sodium storage of a large-scalable carbon anode with an ultralong cycle life. *Advanced Energy Materials*, 8(16):1703159, 2018.
- [32] Shaohua Guo, Yang Sun, Jin Yi, Kai Zhu, Pan Liu, Yanbei Zhu, Guo-zhen Zhu, Mingwei Chen, Masayoshi Ishida, and Haoshen Zhou. Understanding sodium-ion diffusion in layered p2 and p3 oxides via experiments and first-principles calculations: a bridge between crystal structure and electrochemical performance. *NPG Asia Materials*, 8(4):e266–e266, 2016.
- [33] Miao Liu, Ziqin Rong, Rahul Malik, Pieremanu-ele Canepa, Anubhav Jain, Gerbrand Ceder, and Kristin A Persson. Spinel compounds as multivalent battery cathodes: a systematic evaluation based on ab initio calculations. *Energy & Environmental Science*, 8(3):964–974, 2015.
- [34] Ramesh K Guduru and Juan C Icaza. A brief review on multivalent intercalation batteries with aqueous electrolytes. *Nanomaterials*, 6(3):41, 2016.

- [35] Wei Xing, Dongfeng Du, Tonghui Cai, Xiaochen Li, Jin Zhou, Yongming Chai, Qingzhong Xue, and Zifeng Yan. Carbon-encapsulated coke nanoparticles derived from metal-organic frameworks as advanced cathode material for al-ion battery. *Journal of Power Sources*, 401: 6–12, 2018.
- [36] Hao Chen, Fan Guo, Yingjun Liu, Tieqi Huang, Bingna Zheng, Nimroth Ananth, Zhen Xu, Weiwei Gao, and Chao Gao. A defect-free principle for advanced graphene cathode of aluminum-ion battery. *Advanced materials*, 29(12):1605958, 2017.
- [37] Leyuan Zhang, Liang Chen, Hao Luo, Xufeng Zhou, and Zhaoping Liu. Large-sized few-layer graphene enables an ultrafast and long-life aluminum-ion battery. *Advanced Energy Materials*, 7(15):1700034, 2017.
- [38] Tonghui Cai, Lianming Zhao, Haoyu Hu, Tongge Li, Xiaochen Li, Sheng Guo, Yanpeng Li, Qingzhong Xue, Wei Xing, Zifeng Yan, et al. Stable coke 2/carbon nanodice@ reduced graphene oxide composites for high-performance rechargeable aluminum-ion batteries. *Energy & Environmental Science*, 11(9):2341–2347, 2018.
- [39] Pieremanuele Canepa, Gopalakrishnan Sai Gautam, Daniel C Hannah, Rahul Malik, Miao Liu, Kevin G Gallagher, Kristin A Persson, and Gerbrand Ceder. Odyssey of multivalent cathode materials: open questions and future challenges. *Chemical reviews*, 117(5):4287–4341, 2017.
- [40] John Emsley. *Nature's building blocks: an AZ guide to the elements*. Oxford University Press, 2011.
- [41] Zhonghua Zhang, Shamu Dong, Zili Cui, Aobing Du, Guicun Li, and Guanglei Cui. Rechargeable magnesium batteries using conversion-type cathodes: A perspective and minireview. *Small Methods*, 2(10):1800020, 2018.
- [42] Claudiu B Bucur. *Challenges of a rechargeable magnesium battery: a guide to the viability of this post lithium-ion battery*. Springer, 2017.
- [43] Rachel Davidson, Ankit Verma, David Santos, Feng Hao, Coleman Fincher, Sisi Xiang, Jonathan Van Buskirk, Kelvin Xie, Matt Pharr, Partha P Mukherjee, et al. Formation of magnesium dendrites during electrodeposition. *ACS Energy Letters*, 4(2):375–376, 2018.
- [44] E Levi, MD Levi, O Chasid, and D Aurbach. A review on the problems of the solid state ions diffusion in cathodes for rechargeable mg batteries. *Journal of Electroceramics*, 22(1-3):13–19, 2009.
- [45] Honglei Shuai, Jing Xu, and Kejing Huang. Progress in retrospect of electrolytes for secondary magnesium batteries. *Coordination Chemistry Reviews*, 422:213478, 2020.

- [46] Shuangshuang Tan, Fangyu Xiong, Junjun Wang, Qinyou An, and Liqiang Mai. Crystal regulation towards rechargeable magnesium battery cathode materials. *Materials Horizons*, 7(8):1971–1995, 2020.
- [47] Chaolin You, Xiongwei Wu, Xinhai Yuan, Yuhui Chen, Lili Liu, Yusong Zhu, Lijun Fu, Yuping Wu, Yu-Guo Guo, and Teunis van Ree. Advances in rechargeable mg batteries. *Journal of Materials Chemistry A*, 2020.
- [48] Yanliang Liang, Rujun Feng, Siqi Yang, Hua Ma, Jing Liang, and Jun Chen. Rechargeable mg batteries with graphene-like mos<sub>2</sub> cathode and ultrasmall mg nanoparticle anode. *Advanced Materials*, 23(5):640–643, 2011.
- [49] Jiazheng Niu, Hui Gao, Wensheng Ma, Fakui Luo, Kuibo Yin, Zhangquan Peng, and Zhonghua Zhang. Dual phase enhanced superior electrochemical performance of nanoporous bismuth-tin alloy anodes for magnesium-ion batteries. *Energy Storage Materials*, 14:351–360, 2018.
- [50] Doron Aurbach, Z Lu, Alex Schechter, Yossef Gofer, H Gizbar, R Turgeman, Y Cohen, Mordechay Moshkovich, and El Levi. Prototype systems for rechargeable magnesium batteries. *Nature*, 407(6805):724–727, 2000.
- [51] Nobuko Yoshimoto, Mami Matsumoto, Minato Egashia, and Masayuki Morita. Mixed electrolyte consisting of ethylmagnesiumbromide with ionic liquid for rechargeable magnesium electrode. *Journal of Power Sources*, 195(7):2096–2098, 2010.
- [52] Prem Wicram Jaschin, Yirong Gao, Yao Li, and Shou-Hang Bo. A materials perspective on magnesium-ion-based solid-state electrolytes. *Journal of Materials Chemistry A*, 8(6):2875–2897, 2020.
- [53] Partha Saha, Prashanth H Jampani, Moni K Datta, Daeho Hong, Bharat Gattu, Prasad Patel, Karan S Kadakia, Ayyakkannu Manivannan, and Prashant N Kumta. A rapid solid-state synthesis of electrochemically active chevrel phases (mo<sub>6</sub>t<sub>8</sub>; t= s, se) for rechargeable magnesium batteries. *Nano Research*, 10(12):4415–4435, 2017.
- [54] Doron Aurbach, Gurukar Shivappa Suresh, Elena Levi, Ariel Mitelman, Oren Mizrahi, Orit Chusid, and Michela Brunelli. Progress in rechargeable magnesium battery technology. *Advanced Materials*, 19(23):4260–4267, 2007.
- [55] E Levi. E. lancry, a. mitelman, d. aurbach, o. isnard, d. jurado. *Chem. Mater*, 18:3705, 2006.
- [56] E Levi and E Lancry. a. mitelman, d. aurbach, g. ceder, d. morgan, and o. isnard. *Chem. Mater*, 18:5492–5503, 2006.
- [57] Eli Lancry, E Levi, Y Gofer, MD Levi, and D Aurbach. The effect of milling on the performance

- of a  $\text{Mo}_6\text{S}_8$  chevrel phase as a cathode material for rechargeable Mg batteries. *Journal of Solid State Electrochemistry*, 9(5):259–266, 2005.
- [58] Seung-Hyun Choi, Jeom-Soo Kim, Sang-Gil Woo, Woosuk Cho, Sun Yong Choi, Jungkyu Choi, Kyu-Tae Lee, Min-Sik Park, and Young-Jun Kim. Role of Cu in  $\text{Mo}_6\text{S}_8$  and Cu mixture cathodes for magnesium ion batteries. *ACS applied materials & interfaces*, 7(12):7016–7024, 2015.
- [59] Minglei Mao, Tao Gao, Singyuk Hou, and Chunsheng Wang. A critical review of cathodes for rechargeable Mg batteries. *Chemical Society Reviews*, 47(23):8804–8841, 2018.
- [60] RENtaL Enjalbert and JEAN Galy. A refinement of the structure of  $\text{V}_2\text{O}_5$ . *Acta Crystallographica Section C: Crystal Structure Communications*, 42(11):1467–1469, 1986.
- [61] Petr Novak and Johann Desilvestro. Electrochemical insertion of magnesium in metal oxides and sulfides from aprotic electrolytes. *Journal of The Electrochemical Society*, 140(1):140, 1993.
- [62] Lifang Jiao, Huatang Yuan, Yuchang Si, Yijing Wang, Jiansheng Cao, Xiuling Gao, Ming Zhao, Xingdi Zhou, and Yongmei Wang. Electrochemical insertion of magnesium in open-ended vanadium oxide nanotubes. *Journal of power sources*, 156(2):673–676, 2006.
- [63] Niya Sa, Hao Wang, Danielle L Proffit, Albert L Lipson, Baris Key, Miao Liu, Zhenxing Feng, Timothy T Fister, Yang Ren, Cheng-Jun Sun, et al. Is alpha- $\text{V}_2\text{O}_5$  a cathode material for Mg insertion batteries? *Journal of Power Sources*, 323:44–50, 2016.
- [64] Gregory Gershinsky, Hyun Deog Yoo, Yosef Gofer, and Doron Aurbach. Electrochemical and spectroscopic analysis of  $\text{Mg}^{2+}$  intercalation into thin film electrodes of layered oxides:  $\text{V}_2\text{O}_5$  and  $\text{MnO}_3$ . *Langmuir*, 29(34):10964–10972, 2013.
- [65] Nupur Nikkan Sinha and N Munichandraiah. Electrochemical conversion of  $\text{LiMn}_2\text{O}_4$  to  $\text{MgMn}_2\text{O}_4$  in aqueous electrolytes. *Electrochemical and Solid State Letters*, 11(11):F23, 2008.
- [66] Congli Yuan, Ying Zhang, Yue Pan, Xinwei Liu, Guiling Wang, and Dianxue Cao. Investigation of the intercalation of polyvalent cations ( $\text{Mg}^{2+}$ ,  $\text{Zn}^{2+}$ ) into  $\lambda\text{-MnO}_2$  for rechargeable aqueous battery. *Electrochimica Acta*, 116:404–412, 2014.
- [67] Chen Ling, Debasish Banerjee, Wei Song, Minjuan Zhang, and Masaki Matsui. First-principles study of the magnesiation of olivines: redox reaction mechanism, electrochemical and thermodynamic properties. *Journal of Materials Chemistry*, 22(27):13517–13523, 2012.
- [68] ES Fois, M Sprik, and M Parrinello. Properties of supercritical water: an ab initio simulation. *Chemical physics letters*, 223(5-6):411–415, 1994.

- [69] Robert K Szilagyi and Mark A Winslow. On the accuracy of density functional theory for iron—sulfur clusters. *Journal of computational chemistry*, 27(12):1385–1397, 2006.
- [70] Reiner M Dreizler and Eberhard KU Gross. *Density functional theory: an approach to the quantum many-body problem*. Springer Science & Business Media, 2012.
- [71] Enrico Fermi. Eine statistische methode zur bestimmung einiger eigenschaften des atoms und ihre anwendung auf die theorie des periodischen systems der elemente. *Zeitschrift für Physik*, 48(1-2):73–79, 1928.
- [72] Barry Simon. Classical boundary conditions as a technical tool in modern mathematical physics. *Advances in Mathematics*, 30(3):268–281, 1978.
- [73] P Hohenberg and W Kohn. Inhomogeneous electron gøs. *Physical Review r-36*, pages 8864–8871, 1964.
- [74] Lu Jeu Sham and Walter Kohn. One-particle properties of an inhomogeneous interacting electron gas. *Physical Review*, 145(2):561, 1966.
- [75] DR Hamann. H 2 o hydrogen bonding in density-functional theory. *Physical review B*, 55(16):R10157, 1997.
- [76] Hannes Jónsson, Greg Mills, and Karsten W Jacobsen. Nudged elastic band method for finding minimum energy paths of transitions. 1998.
- [77] Graeme Henkelman, Gísli Jóhannesson, and Hannes Jónsson. Methods for finding saddle points and minimum energy paths. In *Theoretical methods in condensed phase chemistry*, pages 269–302. Springer, 2002.
- [78] Graeme Henkelman and Hannes Jónsson. A dimer method for finding saddle points on high dimensional potential surfaces using only first derivatives. *The Journal of chemical physics*, 111(15):7010–7022, 1999.
- [79] Alexander Urban, Dong-Hwa Seo, and Gerbrand Ceder. Computational understanding of li-ion batteries. *npj Computational Materials*, 2(1):1–13, 2016.
- [80] John P Perdew, Kieron Burke, and Matthias Ernzerhof. Generalized gradient approximation made simple. *Physical review letters*, 77(18):3865, 1996.
- [81] Kyuho Lee, Éamonn D Murray, Lingzhu Kong, Bengt I Lundqvist, and David C Langreth. Higher-accuracy van der waals density functional. *Physical Review B*, 82(8):081101, 2010.
- [82] S Kiruthika, H Fjellvåg, and P Ravindran. Amphoteric behavior of hydrogen ( $h+ 1$  and  $h- 1$ ) in complex hydrides from van der waals interaction-including ab initio calculations. *Journal of Materials Chemistry A*, 7(11):6228–6240, 2019.

- [83] Stefan Grimme. Accurate description of van der waals complexes by density functional theory including empirical corrections. *Journal of computational chemistry*, 25(12):1463–1473, 2004.
- [84] Ana Suarez Negreira, Shela Aboud, and Jennifer Wilcox. Surface reactivity of v<sub>2</sub>o<sub>5</sub>(001): Effects of vacancies, protonation, hydroxylation, and chlorination. *Physical Review B*, 83(4):045423, 2011.
- [85] Gregory Gershinsky, Hyun Deog Yoo, Yosef Gofer, and Doron Aurbach. Electrochemical and spectroscopic analysis of mg<sup>2+</sup> intercalation into thin film electrodes of layered oxides: V<sub>2</sub>O<sub>5</sub> and mOO<sub>3</sub>. *Langmuir*, 29(34):10964–10972, 2013.
- [86] C Delmas, H Cognac-Auradou, JM Cocciantelli, M Menetrier, and JP Doumerc. The lixv<sub>2</sub>O<sub>5</sub> system: An overview of the structure modifications induced by the lithium intercalation. *Solid State Ionics*, 69(3-4):257–264, 1994.
- [87] JS Braithwaite, CRA Catlow, JD Gale, and JH Harding. Lithium intercalation into vanadium pentoxide: a theoretical study. *Chemistry of materials*, 11(8):1990–1998, 1999.
- [88] Thomas D Gregory, Ronald J Hoffman, and Richard C Winterton. Nonaqueous electrochemistry of magnesium: applications to energy storage. *Journal of The Electrochemical Society*, 137(3):775, 1990.
- [89] C Delmas, H Cognac-Auradou, JM Cocciantelli, M Menetrier, and JP Doumerc. The lixv<sub>2</sub>O<sub>5</sub> system: An overview of the structure modifications induced by the lithium intercalation. *Solid State Ionics*, 69(3-4):257–264, 1994.
- [90] JS Braithwaite, CRA Catlow, JD Gale, and JH Harding. Lithium intercalation into vanadium pentoxide: a theoretical study. *Chemistry of materials*, 11(8):1990–1998, 1999.
- [91] RJ Cava, A Santoro, DW Murphy, SM Zahurak, RM Fleming, P Marsh, and RS Roth. The structure of the lithium-inserted metal oxide δliv<sub>2</sub>O<sub>5</sub>. *Journal of solid state chemistry*, 65(1):63–71, 1986.
- [92] Gregory Gershinsky, Hyun Deog Yoo, Yosef Gofer, and Doron Aurbach. Electrochemical and spectroscopic analysis of mg<sup>2+</sup> intercalation into thin film electrodes of layered oxides: V<sub>2</sub>O<sub>5</sub> and mOO<sub>3</sub>. *Langmuir*, 29(34):10964–10972, 2013.
- [93] Yanwei Li, Jinhuan Yao, Evan Uchaker, Ming Zhang, Jianjun Tian, Xiaoyan Liu, and Guozhong Cao. Sn-doped v<sub>2</sub>O<sub>5</sub> film with enhanced lithium-ion storage performance. *The Journal of Physical Chemistry C*, 117(45):23507–23514, 2013.
- [94] Zhuoyu Li, Changkun Zhang, Chaofeng Liu, Haoyu Fu, Xihui Nan, Kan Wang, Xinyuan Li, Wenda Ma, Xianmao Lu, and Guozhong Cao. Enhanced electrochemical properties of sn-doped v<sub>2</sub>O<sub>5</sub> as a cathode material for lithium ion batteries. *Electrochimica Acta*, 222:1831–1838, 2016.

- [95] Yinlu Sun, Zhiping Xie, and Yanwei Li. Enhanced lithium storage performance of v<sub>2</sub>o<sub>5</sub> with oxygen vacancy. *RSC advances*, 8(69):39371–39376, 2018.
- [96] V Shklover, T Haibach, F Ried, R Nesper, and P Novak. Crystal structure of the product of mg<sup>2+</sup> insertion into v<sub>2</sub>o<sub>5</sub>single crystals. *Journal of solid state chemistry*, 123(2):317–323, 1996.
- [97] Petr Nόvák, Valery Shklover, and Reinhard Nesper. Magnesium inserttion in vanadium oxides: a structural study. *Zeitschrift für Physikalische Chemie*, 185(1):51–68, 1994.
- [98] N Van Hieu and D Lichtman. Bandgap radiation induced photodesorption from v<sub>2</sub>o<sub>5</sub> powder and vanadium oxide surfaces. *Journal of Vacuum Science and Technology*, 18(1):49–53, 1981.
- [99] V Eyert and K-H Höck. Electronic structure of v<sub>2</sub>o<sub>5</sub>: role of octahedral deformations. *Physical Review B*, 57(20):12727, 1998.
- [100] Jürgen Spitaler, Eugene Ya Sherman, and Claudia Ambrosch-Draxl. First-principles study of phonons, optical properties, and raman spectra in mgv<sub>2</sub>o<sub>5</sub>. *Physical Review B*, 78(6):064304, 2008.
- [101] Bo Zhou, Hui Shi, Rongfang Cao, Xiaodong Zhang, and Zhenyi Jiang. Theoretical study on the initial stage of a magnesium battery based on a v<sub>2</sub>o<sub>5</sub> cathode. *Physical Chemistry Chemical Physics*, 16(34):18578–18585, 2014.